Swinging Motion of a Kite with Suspended Control Unit Flying Turning Manoeuvres

Mark Schelbergen[1] and Roland Schmehl[1]

[1]Faculty of Aerospace Engineering, Delft University of Technology, 2629 HS Delft, Netherlands

Correspondence: Mark Schelbergen (m.schelbergen@tudelft.nl)

Abstract. The flexible membrane kite employed by some airborne wind energy systems carries a suspended control unit capable of inducing a characteristic pitch and roll swinging motion during sharp turning manoeuvres. This paper assesses how accurately a two-point kite model approximates this swinging motion with two approaches: approximated as a transition through steady-rotation states and solved dynamically. The kite model comprises the rigidly linked point masses of the control unit and wing and extends a discretised tether model. The motion of the wing point mass is constrained to a figure-of-eight manoeuvre from the flight data of an existing prototype. The associated swinging motion of the kite is inferred from the attitude of the rigid link element. The computed attitude is compared against the measurements of two sensors mounted to the wing, which record varying pitch angles during the turns. The pitch and roll angles computed with the two approaches are similar during the straight sections of the figure-of-eight manoeuvre and match the measured angles within three degrees. Contrastingly, the two approaches exhibit systematic differences during the turns. Since a two-point kite model resolves the roll, the lift force may tilt along with the kite to drive turns. Hence, intricate centripetal force modelling is avoided, as seen in a single-point kite model. Furthermore, the two-point kite model complements the aerodynamic model as it allows computing the angle of attack of the wing by resolving the pitch. These characteristics improve the generalization of the kite model with little additional computational effort.

1 Introduction

Pumping airborne wind energy (AWE) systems with flexible membrane kites are reaching a technology readiness level suitable for first commercial applications. Two prominent examples are the leading developers SkySails Power GmbH using ram-air kites and Kitepower B.V. using leading-edge inflatable (LEI) kites Vermillion et al. (2021); Fagiano et al. (2022). Both systems employ a single tether and a suspended kite control unit (KCU) for actuating the wing, as illustrated in Figure 1. At the present stage of development, AWE systems are not optimised yet in terms of power production. Instead, the priority is improving operational reliability and demonstrating long-term operation, as well as learning how the systems perform in different wind environments Salma et al. (2019). This knowledge will be crucial for designing the next generation of systems with increased power output.

Performance models estimate the energy generation of a specific system in a varying wind environment over extended periods of time. The most simple and computationally efficient models extend Loyd's analytic theory of tethered flight Loyd

Figure 1. AWE system of Kitepower B.V. with a 60 m^2 kite and ground station integrated in a standard 20 ft container in operation on the Caribbean island Aruba in October 2021 (photo courtesy of Kitepower B.V.).

(1980) and do not touch upon turning. In a next level of model refinement, quasi-steady models prescribe a parameterised flight path to increase the resolution of the flight path. Thereby, they account for the effect of turning but do not necessarily describe the mechanism that makes the kite turn. Alternatively, dynamic models require incorporating a turning mechanism and can be applied in an optimal control problem (OCP) to find an optimal realistic flight path. The simpler models represent

30 the kite as a single point mass or rigid body and assume a straight tether with its mass and drag lumped to the kite. More refined models also resolve tether sag induced by lateral forces on the tether, such as gravity, centrifugal force, and aerodynamic drag. This can be conveniently done by discretising the tether. Typically, the tether is represented with lumped masses connected with rigid links or spring-damper elements Gohl and Luchsinger (2013); Fechner et al. (2015); Rapp et al. (2019); Williams et al. (2007); Zanon et al. (2013). Alternatively, Sánchez-Arriaga et al. (2019) apply a multi-body approach using rigid rods.

35 Fechner et al. (2015) expand the discretisation approach to the kite. The kite is represented with five point masses; four point masses represent the wing, and one additional point mass represents the suspended KCU. A lumped-mass model with spring-damper elements yields a stiff system of differential equations. Solving this system requires a small time step and is prone to numerical instabilities. These models are considered too computationally costly for performance calculation but are used for control system design.

40   To efficiently account for tether elasticity, Williams (2017) solves the 'quasi-static' tether deformation as a subroutine to solving the motion of the kite. Consequently, the loaded tether shape due to gravity, centrifugal force and aerodynamic drag is considered, while the transient motion and longitudinal vibration are neglected. The discretised tether model assumes that the entire airborne system, including tether and kite, jointly rotates around the tether attachment point at the ground. This assumed kinematic relationship works well for near-straight flights but is not representative during turning manoeuvres.

45   The choice of the kite model determines the level of abstraction required to introduce steering forces as demonstrated in the work of Fechner et al. (2015). The kite acquires its turning capabilities by manipulating the aerodynamic force generated by the wing to generate a centripetal force. In the single-point model of a LEI kite, the actuation is incorporated by exerting a lateral force to the point mass proportional to the steering input. A rather high maximum side force coefficient of 2.59 is found empirically. The five-point kite model allows for a more realistic incorporation of the side force with the lift forces of the kite

50   tips. The lift coefficients at the tips do not exceed 1.1.

    In reality, the deformation of the wing due to steering input is not as simple as suggested by the latter aerodynamic models. The LEI kite of Kitepower B.V. is steered by pulling the rear bridle lines attached to one side of the wing while loosening the lines on the other side. This asymmetric actuation of the bridle line system makes the wing deform and initiate a turn. Video footage of experiments shed some light on the aero-structural deformation due to steering Schmehl and Oehler (2018).

55   Previous research on the topic has focused mainly on the interaction between the flow and the deforming bridled membrane wing Breukels et al. (2013); Bosch et al. (2013); Geschiere (2014); Duport (2018); Oehler et al. (2018); Thedens (2022); Folkersma (2022); Poland (2022); Cayon (2022). The experimental data also indicates a pronounced dynamic interaction between the wing, the suspended KCU, and the tether during the turning manoeuvre. How much this swinging motion affects the turning behaviour and the power generation of the kite has only recently been studied by Roullier (2020). An improved

60   understanding of this effect would allow for enhancing performance models of flexible membrane kites, designing more precise control algorithms, and ultimately improving the system performance.

    We hypothesize that the roll of a flexible kite induced by the inertia of the suspended KCU has a crucial role in the turns. To investigate this mechanism, we use a discretised tether model extended with a two-point kite model. Instead of solving for the path of the wing, we prescribe a cross-wind flight path from the flight data of Kitepower B.V. This removes the dependency

65   of the model on the aerodynamics of the kite and, thereby, reduces uncertainties. The tether-kite motion is studied using two approaches. The first approximates the motion as a transition through steady-rotation states. The second uses a dynamic model to solve the motion directly. Finally, we discuss the implications of the results for performance modelling for flexible kite systems.

    This paper is organised as follows. In Section 2 the experimental data underlying this study is described. In Section 3 the

70   computational model is outlined. The results are presented in Section 4 and discussed in Section 5. Conclusions are presented in Section 6.

2   Test Flight Data

The data used in the present study was acquired on 8 October 2019 using a 25 m² V3.25B kite of Kitepower, depicted in Figure 2. This kite is a derivative of the TU Delft LEI V3 kite described by Oehler and Schmehl (2019) and illustrated in Figure 3. We use the term kite for the entire assembly of the wing, bridle line system, and suspended control unit. Conservative operational settings were used for this specific flight because its purpose was to test new hard- and software components of the system and to acquire data. The operated kite was substantially smaller and less performant than the 60 m² kite shown in Figure 1 that Kitepower B.V. develops for the commercial 100 kW system Kitepower B.V.. Considering all this, the power output during the test was substantially lower than for the nominal operation of the commercial system.

Figure 2. Fully instrumented V3.25B kite before launch (photo courtesy of Kitepower B.V.).

The published data set Schelbergen et al. (2023) covers approximately three hours of flight time, during which 87 automatic pumping cycles were recorded. With this large data set, statistical insights into the flight behaviour of the kite can be gained. The apparent wind speed was measured with a Pitot tube attached to the front bridle lines at the connection to a power line. This flow sensor is visible in the foreground of Figure 2, also featuring a flow vane to measure the angle of attack. The side slip angle was not measured in this setup. A tether with a diameter of 10 mm was used during the flight test, and onboard electrical power was supplied by a small ram-air turbine, as shown in Peschel et al. (2017).
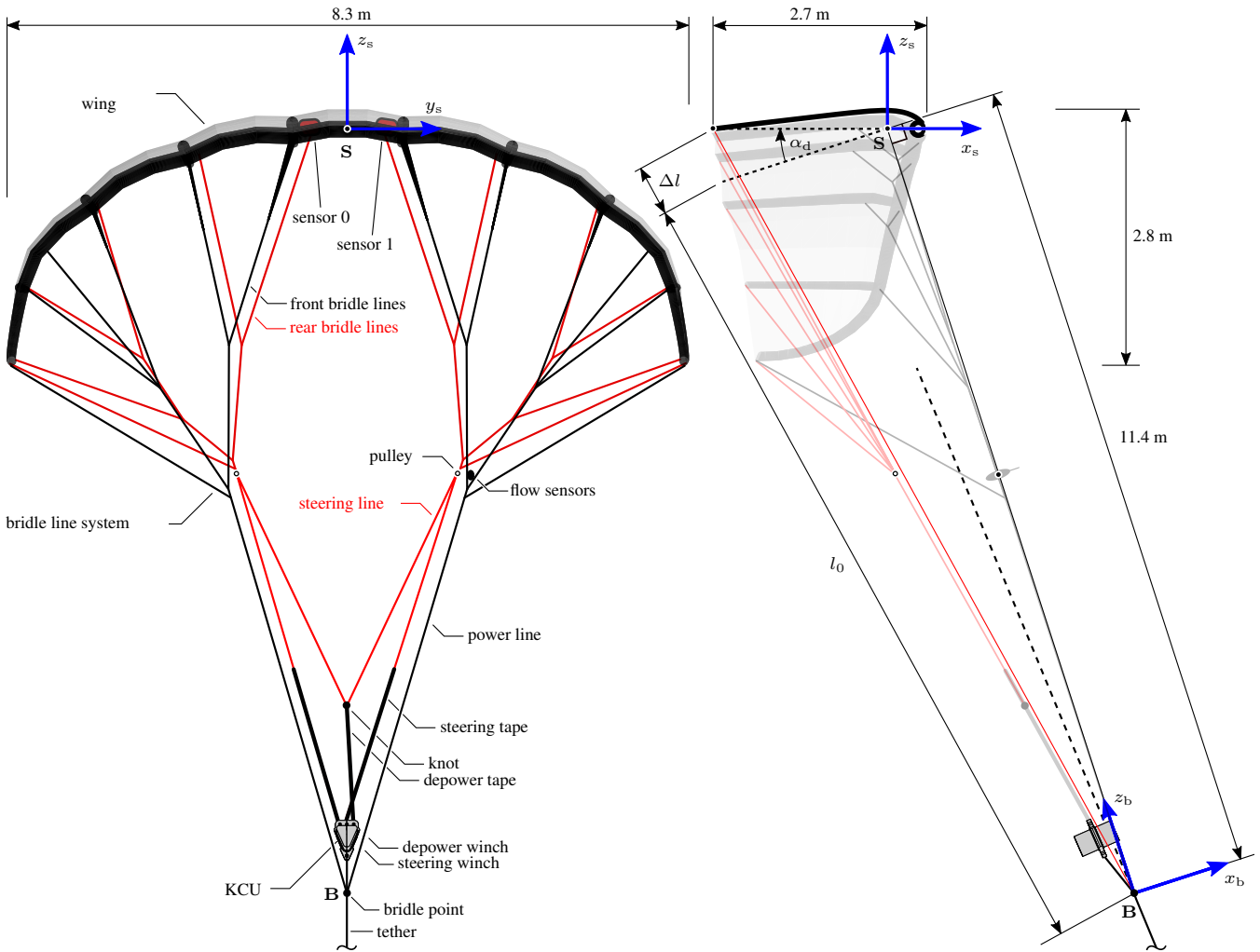
Figure 3. Front-view (left) and side-view (right) of the LEI V3 kite. Also depicted are the sensor reference frame x_s, y_s, z_s, with origin **S** at the point around which the wing pitches when changing the angle of attack, and the bridle reference frame x_b, y_b, z_b with origin at the bridle point **B**. The two Pixhawk® sensors 0 and 1 approximately measure in the sensor reference frame while the relative flow approximately measures in the bridle reference frame. Adapted from Oehler and Schmehl (2019).

We illustrate our analysis using the specific figure-of-eight cross-wind manoeuvre shown in Figure 4, which is part of the 65th pumping cycle of the test flight. Because of the high repeatability of the automatic flight manoeuvres, the other figures of eight of the dataset give similar results. Characteristic reference positions along this manoeuvre are designated to highlight the analysis, listed in Table 1. The kite flies along the trajectory in the direction of increasing reference numbers, i.e., flying upwards on the straight path segments and downwards during the turns. The tether is reeled-out while the kite is flying cross-wind manoeuvres, increasing the radial position of the kite from 276 to 302 m at a height of 150–185 m. The asymmetry

of the trajectory can be attributed to various factors, including misalignment with the wind velocity due to wind veer and imperfections within the system.
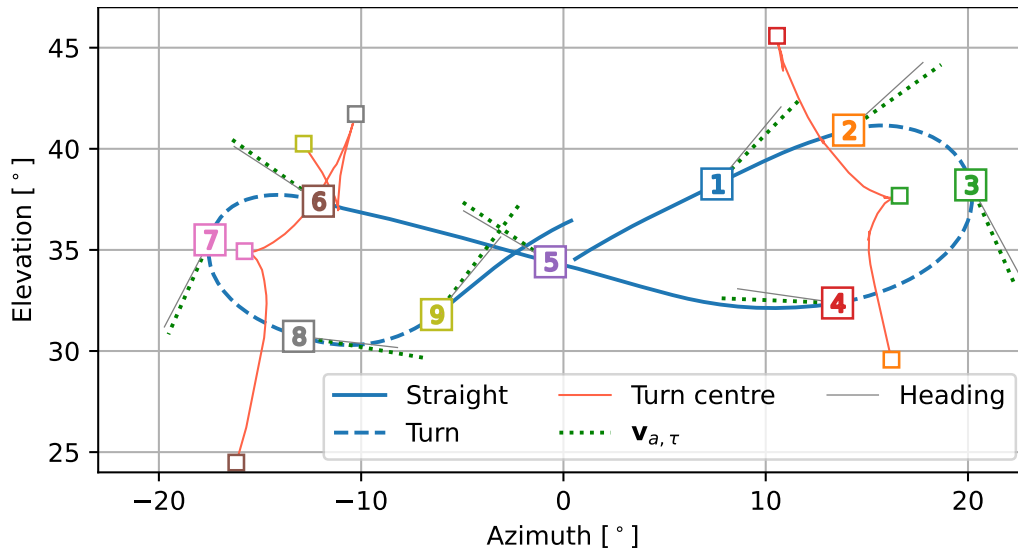
Figure 4. The studied figure-of-eight cross-wind manoeuvre depicted with respect to the wind reference frame, shown in Figure B1. The flight path is composed of straight (solid blue) and turn (dashed blue) line segments. Reference positions 1 to 9 are designated along the path in flight direction. For the two turns, the changing position of the turn centre is tracked with the red lines. The turn-centre markers pair with the numbered path markers of the same colour. The dotted lines depict the modelled apparent wind velocity. Alongside the apparent wind velocity lines, the solid lines depict the heading inferred from the attitude measurements of sensor 1.

Table 1. Timestamps of the reference positions along the figure-of-eight path shown in Figure 4, starting at 29.9 s and ending at 51.2 s in the 65th pumping cycle.

Instance label	1	2	3	4	5	6	7	8	9
Time [s]	31.9	33.9	35.6	37.5	41.0	44.5	46.2	47.6	49.1

The measured position and attitude of the wing and the tether force are used as input for our calculations. For this flight test, two Pixhawk® sensor units were mounted to the wing, one on each of the two struts adjacent to the symmetry plane of the kite. The units are each equipped with an IMU and a GPS sensor for recording position and attitude. The default Kalman filter implementation was used to enhance the quality of the measurements. The grey lines in Figure 4 show the heading of the kite at the reference positions inferred from sensor 1.

Furthermore, the tether force and the reel-out speed measured at the ground station are used as input. Comparing the tether reel-out speed to the position of the wing indicates anomalies in the recorded wing position that manifest as unrealistically large

jumps in radial position predominately occurring during right turns. Appendix A describes how the anomalies are removed to provide a consistent input for the dynamic simulation.

For simplicity, the wind velocity is assumed to be uniform and constant. The average wind speed measured at the ground for the reference pumping cycle is approximately 7 m s^{-1}. Based on the estimated wind shear, the wind speed at the kite is

105   assumed to be 10 m s^{-1}. The dotted green lines in Figure 4 show the projection of the apparent wind velocity approximated with

$$\mathbf{v}_a = \mathbf{v}_\text{w} - \mathbf{v}_\text{k}, \tag{1}$$

in which $\mathbf{v}_\text{w} = [10\ 0\ 0]$ is the wind velocity and $\mathbf{v}_\text{k}$ is the measured kite velocity. In case of zero side slip, the heading of the kite would align with the apparent wind velocity. However, the approximation of the apparent wind velocity lacks the necessary

110   precision to assess the side slip. Moreover, the side slip angle was not measured during the flight test and therefore, assessing the side slip is out of scope.

3   Computational Modelling

The flight behaviour along the figure of eight described in the previous section is analysed with two different computational implementations of a two-point kite model with a discretised tether model. The first approximates the tether-kite motion as a

115   transition through steady-rotation states. The second uses a dynamic model to solve the motion directly.

3.1   Tether-kite model

When solving the unconstrained kite motion, an important model element is the calculation of the aerodynamic loads of the kite, relying on an accurate description of its rotational behaviour. Accordingly, a key deficiency of representing the kite as a single point mass is that it relies on kinematic assumptions to describe its rotational behaviour. The two-point model developed

120   for the present analysis accounts for the two distinct mass concentrations of the wing and the KCU. During cross-wind flight, the bridle line system is tensioned by the aerodynamic force acting on the wing. Accordingly, the two point masses stay at a constant distance, considering that the effect of wing actuation, including deformation, is negligible. From a modelling perspective, the two point masses at a constant distance are similar to a rigid body model, with rotational inertia in pitch and roll, but not in yaw. Although not required for the current analysis in which the kite aerodynamics are excluded, the yaw

125   motion still needs to be described with kinematic assumptions in case of solving the full motion. The two-point kite model can be added in a straightforward way to a discretised tether model as an additional final segment. An example with five tether segments of equal length l_j and a kite segment of length l_b is shown in Figure 5.

To account for a varying length l_t and mass m_t of the deployed tether, the segment lengths and point masses are updated every instance according to

130    $$l_\text{j} = \frac{l_\text{t}}{N}, \tag{2}$$
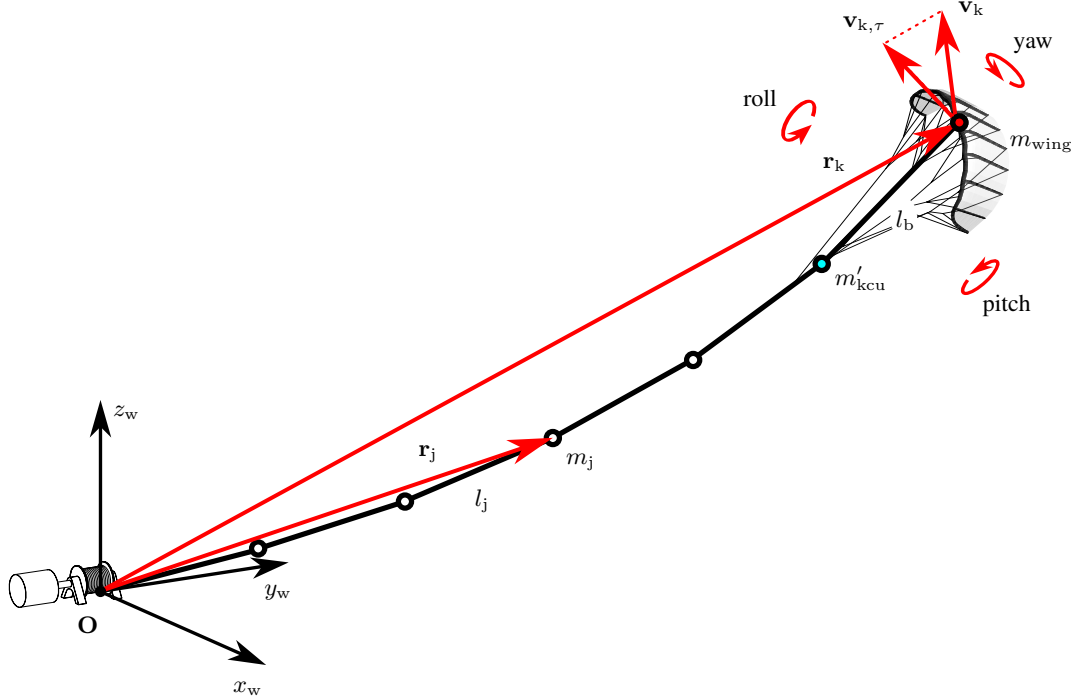
Figure 5. Two-point model of the kite added to a tether discretised by $N = 5$ tether elements. The position $\mathbf{r}_k$ and flight velocity $\mathbf{v}_k$ of the kite are defined as the position and velocity of the point $\mathbf{S}$ where the sensor units are attached to the wing, see Figure 4. Also shown is the tangential kite velocity component $\mathbf{v}_{k,\tau}$ (perpendicular to $\mathbf{r}_k$) and the wind reference frame x_w, y_w, z_w with origin at the tether attachment point $\mathbf{O}$ on the ground.

$$m_j = \frac{m_t}{N}, \tag{3}$$

where N is the constant number of segments. The point mass representing the KCU is determined as

$$m'_{kcu} = m_{kcu} + \frac{m_j}{2}. \tag{4}$$

We use the approximations of Zanon et al. (2013) to determine the aerodynamic drag acting on the point masses representing

135 the tether

$$\mathbf{D}_{t,j} = \frac{1}{2}\rho \|\mathbf{v}_{a,j}\| \mathbf{v}_{a,j} C_{D,t} l_j d_t, \qquad \text{with} \quad j = 1, \ldots, N, \tag{5}$$

where ρ is the air density, $\mathbf{v}_{a,j}$ are the local apparent wind velocities at the jth point mass, $C_{D,t}$ is the tether drag coefficient, and d_t is the tether diameter.

Additional to half the drag of the last tether element, the drag $\mathbf{D}_{kcu}$ of the KCU is acting on the point mass below the wing.

140 Consequently, the total drag acting on the KCU point mass is

$$\mathbf{D}'_{kcu} = \mathbf{D}_{kcu} + \mathbf{D}_{t,kcu} = \frac{1}{2}\rho \|\mathbf{v}_{a,kcu}\| \mathbf{v}_{a,kcu} C_{D,kcu} A_{kcu} + \frac{\mathbf{D}_{t,N}}{2}, \tag{6}$$

in which $\mathbf{v}_{\mathrm{a,kcu}}$ is the apparent wind velocity at the point mass. The frontal area of the KCU is denoted as A_{kcu} and the drag coefficient as $C_{\mathrm{D,kcu}}$. The bridle and ram-air turbine drag are not included as separate terms but are lumped to the KCU drag. The values of physical parameters are listed in Table 2.

Table 2. Physical parameters of the airborne system model.

v_{w}	m_{kcu}	m_{wing}	l_{b}	ρ	d_{t}	$C_{\mathrm{D,t}}$	A_{kcu}	$C_{\mathrm{D,kcu}}$
$10\,\mathrm{m\,s^{-1}}$	$25\,\mathrm{kg}$	$14.2\,\mathrm{kg}$	$11.5\,\mathrm{m}$	$1.225\,\mathrm{kg\,m^{-3}}$	$10\,\mathrm{mm}$	1.1	$0.25\,\mathrm{m^2}$	1.0

145 Equation (5) does not account for any variation of the apparent wind velocity along the tether element and is only a reasonable approximation when using many tether elements. For single-element use, the alternative expression for the tether drag contribution in Equation (6) (last term) better preserves the moment of the tether drag around the ground station

$$\mathbf{D}_{\mathrm{t,kcu}} = \frac{1}{8}\,\rho\,\|\mathbf{v}_{\mathrm{a,kcu}}\|\,\mathbf{v}_{\mathrm{a,kcu}}\,C_{\mathrm{D,t}}\,l_{\mathrm{t}}\,d_{\mathrm{t}}\,. \tag{7}$$

3.2 Steady-rotation states

150 The subroutine for solving the 'quasi-static' tether shape proposed by Williams (2017) is adopted in the present analysis to assess the swinging motion of the kite. With an initial guess of the tether length and orientation of the lower segment, the corresponding tether shape is determined using a shooting method. The positions of the point masses are determined one by one, starting with the lowest point mass and moving up towards the last point mass located at the tether end. From the force balance on a particular point mass (at the intersection of two tether elements), the position of the next point mass is inferred.
155 This force balance consists of the tensile forces, drag, weight, and centrifugal force. Given the tensile force acting on the tether element below the point mass, only the tensile force acting on the tether element above remains unknown and is solved. The direction of this force dictates the axial direction of the corresponding tether element. Together with the length of a tether element, the axial direction yields the position of the next point mass at the end of that element. By repeating this calculation for each point mass, the position of the kite is obtained given the measured tether force at the ground. A least squares optimisation
160 is employed to find the tether shape for which the upper tether end coincides with the position of the wing. Consult Williams (2017) for more details.

To allow for calculating the loads, the velocities and accelerations of the point masses are approximated by assuming that they collectively rotate steadily around the tether attachment point at the ground, similar to a rigid body. The corresponding kinematic relationships for the velocity $\mathbf{v}_{\mathrm{j}}$ an acceleration $\mathbf{a}_{\mathrm{j}}$ for the jth point mass are

165
$$\mathbf{v}_{\mathrm{j}} = \boldsymbol{\omega} \times \mathbf{r}_{\mathrm{j}}, \qquad \text{with} \quad j = 1,\dots,N, \tag{8}$$

$$\mathbf{a}_{\mathrm{j}} = \boldsymbol{\omega} \times \mathbf{v}_{\mathrm{j}}, \qquad \text{with} \quad j = 1,\dots,N. \tag{9}$$

Accordingly, the velocities and accelerations of all point masses are fully described with a single angular velocity $\boldsymbol{\omega}$ and their respective positions $\mathbf{r}_j$. Williams calculates the rotational velocity $\boldsymbol{\omega}_{\text{straight}}$ with

$$\boldsymbol{\omega}_{\text{straight}} = \frac{\mathbf{r}_k \times \mathbf{v}_k}{\|\mathbf{r}_k\|^2} = \frac{\mathbf{r}_k \times \mathbf{v}_{k,\tau}}{\|\mathbf{r}_k\|^2}, \tag{10}$$

170   in which $\mathbf{r}_k$ and $\mathbf{v}_k$ are the position and velocity of the kite, respectively, and $\mathbf{v}_{k,\tau}$ is the tangential component of the kite velocity, shown in Figure 5. The resulting rotational velocity yields a rotation along a great circle on the surface of a sphere as shown in Figure 6.

This great-circle rotation produces accelerations on the point masses pointing towards the tether attachment point, which is representative of the quasi-straight sections of a figure-of-eight manoeuvre. However, during turns, the kite and tether are
175   expected to experience a lateral acceleration. An angular velocity that is representative of turns can be found by replacing the kite position $\mathbf{r}_k$ in Equation (10) with the separation vector between the kite and the turn centre $\mathbf{r}_{\text{turn}}$:

$$\boldsymbol{\omega}_{\text{turn}} = \frac{\mathbf{r}_{\text{turn}}}{\|\mathbf{r}_{\text{turn}}\|^2} \times \mathbf{v}_k. \tag{11}$$

The resulting rotational velocity produces a rotation along a small circle on the surface of a sphere coinciding with the turn of the figure-of-eight manoeuvre as shown in Figure 6.

180   For each turn, the centre is geometrically derived by fitting a circular segment to 1-second-long flight paths projected onto the azimuth-elevation plane. Since the turns are not perfectly circular, the turn centre changes throughout the turns. The changing position of the turn centre is tracked with the red lines in Figure 4. The colour of the marked points on the turn-centre track links them to the wing position markers. The distance between the paired markers gives an indication of the turn radius. The turn-centre track shows that the turn centre moves up throughout the turn and that the turn radius is smallest at the outermost
185   section of the figure of eight.

Calculating the angular velocity during the turns with Equation (11) and during the quasi-straight sections with Equation (10) yields the red line within and outside the grey-shaded intervals, respectively, in Figure 7a. As expected, the corresponding centripetal acceleration of the wing calculated by filling in $\mathbf{r}_k$ into Equations (8–9) is substantially larger during the turns than the measured wing acceleration, as can be observed in Figure 7c.

190   A shortcoming of the previous angular velocity approximations is that they do not consider the measured kite acceleration. An optimisation is used to find the angular velocity that yields the kite velocity and acceleration closest to the measurements using an unweighted least-squares approach. The optimal angular speed is shown with the blue line in Figure 7a. Except for the peak in the middle of the second turn, the estimated and optimised angular speeds agree reasonably well. The optimised angular velocity yields a good approximation of not only the kite velocity but also the acceleration, as can be seen in Figure 7b
195   and c. Therefore, the optimised angular velocity is used to study the swinging motion of the kite.

To conclude, we apply the following model modifications:

– No elasticity of the tether elements is considered;

– We allow for rotations other than great-circle rotations;
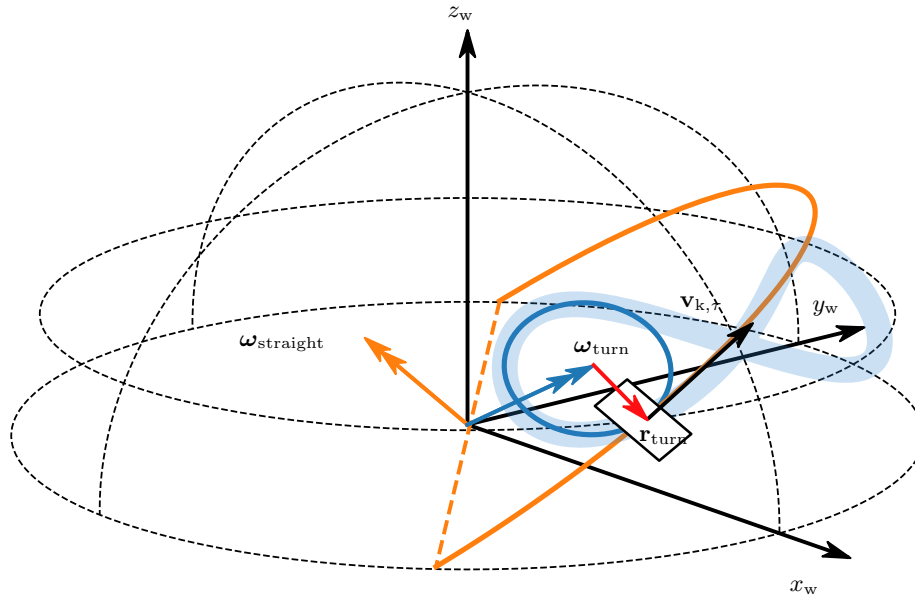
Figure 6. Two possible angular velocities, $\boldsymbol{\omega}_{\text{straight}}$ and $\boldsymbol{\omega}_{\text{turn}}$, that can be deduced from the tangential kite velocity $\mathbf{v}_{\text{k},\tau}$. Their respective steady-rotation flight paths comprise a great circle and coincide with the turn of the figure-of-eight manoeuvre, respectively. The yawed tangential plane depicted as a rectangle represents the kite.

- – The radial velocity of the point masses is neglected;

200   – The drag on the tether elements is determined as a function of the full apparent wind velocity (squared) instead of the velocity perpendicular to the elements for consistency with the dynamic model;

- – A different lumping approach is used for the uppermost tether point mass than for the other tether point masses, i.e., the mass and drag of half a tether element are allocated to the former instead of the mass and drag of a full element;

- – We add an extra element (rigid link) to represent the kite as described in Section 3.1.

205 **3.3 Dynamic model**

The proposed dynamic model is based on the work of Zanon et al. (2013), using non-minimal Cartesian coordinates to reduce the non-linearity of the model formulation. The dynamics of the point masses are included using separate equations and coupled through algebraic constraints. Index reduction is used to make the algebraic variables appear explicitly in the differential equations, enabling more efficient integration.

210   Although the model allows for multiple kite system architectures, we only consider a simple single-tether, single-kite configuration. For brevity, we only present the model formulation with a single tether element. In this simplest form, with one element representing the tether and another element for the kite, the differential-algebraic equations (DAEs) describing the
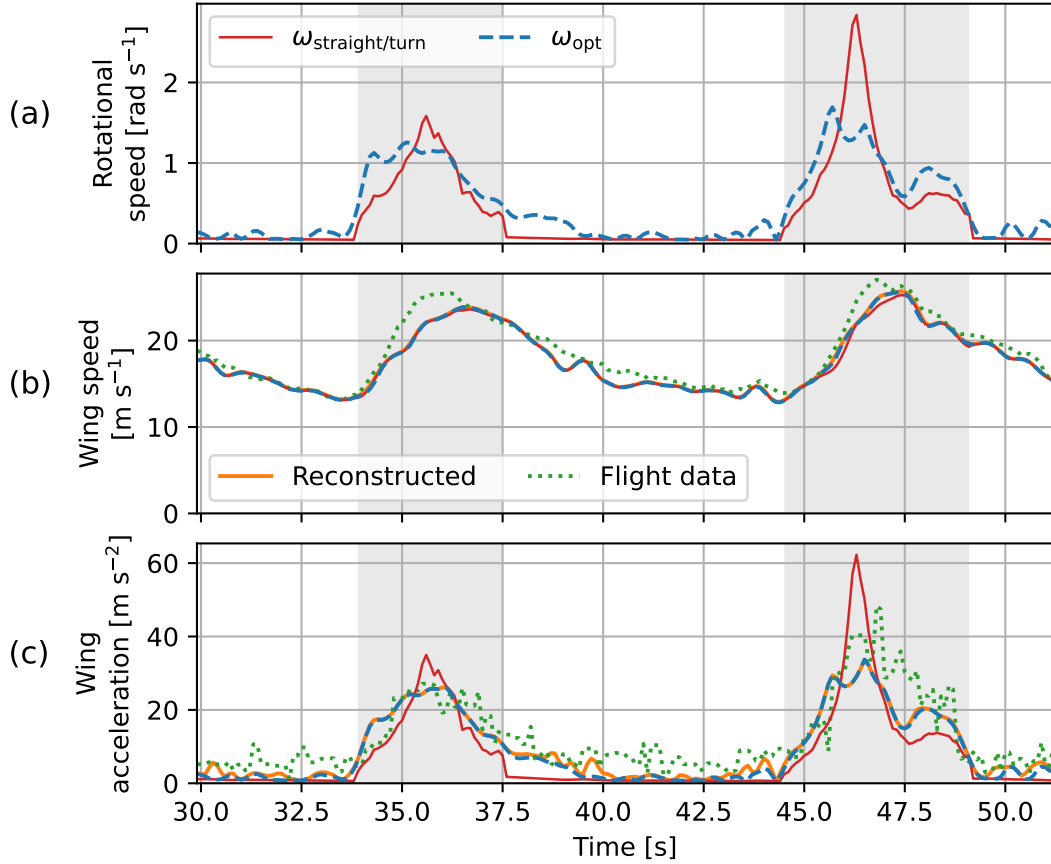
Figure 7. Evaluating the steady-rotation assumption with the different rotational velocities. (**a**) The calculated straight path and turn rotational speed ($\omega_{\mathrm{straight}}$ outside and ω_{turn} inside grey interval) and the rotational speed found using optimisation (ω_{opt}). (**b**, **c**) The wing speed and acceleration from the flight trajectory reconstruction used to infer the rotational velocities, and the wing speeds and accelerations back-calculated with these different rotational velocities. For reference, the original speed and acceleration of the flight data are shown. The shaded intervals indicate the turns.

dynamics read as

$$
\begin{bmatrix}
m'_{\mathrm{kcu}}\mathbf{I}_3 & \mathbf{0}_{3x3} & \mathbf{r}_{\mathrm{kcu}} & \mathbf{r}_{\mathrm{kcu}} - \mathbf{r}_{\mathrm{s}} \\
\mathbf{0}_{3x3} & m_{\mathrm{s}}\mathbf{I}_3 & \mathbf{0}_{3x1} & \mathbf{r}_{\mathrm{s}} - \mathbf{r}_{\mathrm{kcu}} \\
\mathbf{r}_{\mathrm{kcu}} & \mathbf{0}_{1x3} & 0 & 0 \\
\mathbf{r}_{\mathrm{kcu}} - \mathbf{r}_{\mathrm{s}} & \mathbf{r}_{\mathrm{s}} - \mathbf{r}_{\mathrm{kcu}} & 0 & 0
\end{bmatrix}
\begin{bmatrix}
\mathbf{a}_{\mathrm{kcu}} \\
\mathbf{a}_{\mathrm{s}} \\
\lambda_{\mathrm{t}} \\
\lambda_{\mathrm{b}}
\end{bmatrix}
=
\begin{bmatrix}
\mathbf{D}'_{\mathrm{kcu}} - m'_{\mathrm{kcu}}\,g\,\mathbf{1}_z \\
\mathbf{F}_{\mathrm{a,c}} - m_{\mathrm{c}}\,g\,\mathbf{1}_z \\
-\mathbf{v}_{\mathrm{kcu}}^T \mathbf{v}_{\mathrm{kcu}} + \dot{l}_{\mathrm{t}}^2 + l_{\mathrm{t}}\ddot{l}_{\mathrm{t}} \\
-\left(\mathbf{v}_{\mathrm{kcu}} - \mathbf{v}_{\mathrm{s}}\right)^T\left(\mathbf{v}_{\mathrm{kcu}} - \mathbf{v}_{\mathrm{s}}\right)
\end{bmatrix},
\tag{12}
$$

215 in which subscript c denotes wing, t denotes tether, and b denotes bridle. Furthermore, $\mathbf{I}_3$ is the identity matrix, λ is a Lagrangian multiplier, $\mathbf{F}_{\mathrm{a,c}}$ is the aerodynamic force acting on the wing, g is the gravitational constant, and $\mathbf{1}_z^T = [0\ 0\ 1]$. For every additional tether element, one differential and one algebraic equation need to be added to the DAEs. Because of the

index reduction, the following consistency conditions need to be met in order to get a physically consistent solution

$$c_\mathrm{t} = \frac{1}{2}\left(\mathbf{r}_\mathrm{kcu}^T\mathbf{r}_\mathrm{kcu} - l_\mathrm{t}^2\right) = 0, \tag{13}$$

220

$$\dot{c}_\mathrm{t} = \mathbf{r}_\mathrm{kcu}^T\mathbf{v}_\mathrm{kcu} - l_\mathrm{t}\dot{l}_\mathrm{t} = 0, \tag{14}$$

$$c_\mathrm{b} = \frac{1}{2}\left((\mathbf{r}_\mathrm{kcu} - \mathbf{r}_\mathrm{s})^T(\mathbf{r}_\mathrm{kcu} - \mathbf{r}_\mathrm{s}) - l_\mathrm{b}^2\right) = 0, \tag{15}$$

225 $\quad \dot{c}_\mathrm{b} = (\mathbf{v}_\mathrm{kcu} - \mathbf{v}_\mathrm{s})^T(\mathbf{r}_\mathrm{kcu} - \mathbf{r}_\mathrm{s}) = 0. \tag{16}$

In principle, the accelerations and Lagrangian multipliers in Equation (12) can be solved explicitly by inverting the mass matrix and subsequently solving the problem using a regular ordinary differential equation integrator. However, solving the problem using a DAE integrator reduces computational costs substantially, especially when using a large number of tether elements. The DAE is converted to a semi-explicit form and implemented in CasADi Andersson et al. (2019), which comes
230 with the IDAS integrator for DAEs.

To prevent inaccuracies of a kite aerodynamic model interfering with the simulation, we do not solve for the dynamics of the wing but use its acceleration as simulation input. Consequently, the second row in Equation (12) becomes redundant and is dropped for this analysis. Using the wing acceleration as control input is analogous to dragging the tether and kite along with a prescribed motion of the wing. Note that the wing acceleration still has a large effect on the simulation as the wing position
235 and velocity, which follow from integrating the acceleration, remain in the equations.

Additional to the wing acceleration, the model needs the reel-out acceleration of the tether as a control input. Moreover, the initial values for the state variables are required to run a simulation. The state variables of the model are the positions and velocities of the point masses together with the tether length and reel-out speed. Besides the initial tether length, the control input is obtained using the flight trajectory reconstruction described in Appendix A.
240 To sum up, we apply the following model modifications:

- Drag is evaluated directly at the point masses instead of at the centres of the tether elements and evenly distributed over the adjacent point masses;

- The acceleration of the upper end of the kite (wing point mass) is not solved for. Instead, the wing acceleration inferred from measurements is directly imposed;

245 - Also here, we add an extra element (rigid link) to represent the kite as described in Section 3.1.

4 Results

Firstly, the steady-rotation-state approximation is used to study the motion of the tether and kite along the figure of eight. A discretisation by 30 tether segments is compared with a minimal discretisation using only a single tether segment. Secondly, the motion is simulated with the dynamic model using 30 tether segments. Subsequently, the resulting roll and pitch along the

250   figure of eight from the different models are compared with measurements. Finally, the motion of the tether and kite along a full pumping cycle is studied.

4.1 Tether-kite lines computed with steady-rotation states

The steady-rotation-state approximation uses the measured tether force, wing position, and optimised angular velocity to determine the instantaneous positions of the point masses. The line formed by the segments between these point masses

255   is referred to as the tether-kite line. Figure 8 shows the resulting tether-kite lines with 30 tether elements at the reference instances.
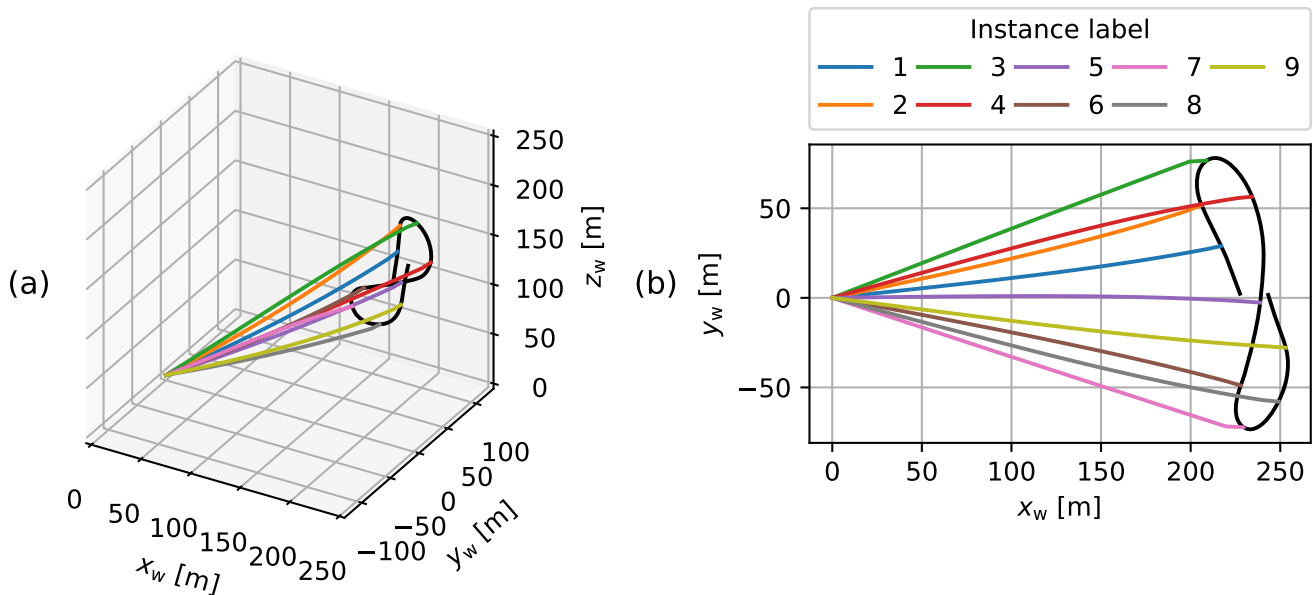
Figure 8. Tether-kite lines for the nine reference instances resulting from the steady-rotation-state approximation with the tether discretised by 30 segments in 3D (**a**) and top-view (**b**).

Variations in the deformation of the tether-kite line are hard to identify with the naked eye in the previous plots. Therefore, the cross-axial displacement is plotted against the radial position for the first five reference instances with the solid lines in Figure 9. The displacement is expressed with respect to the apparent wind velocity of the kite. The largest displacements are

260 found in the down-apparent-wind direction, which can be attributed to the tether drag. In contrast, tether drag hardly contributes to the cross-apparent-wind displacement. The resistance to turn, or the inertia, mostly contributes to the cross-apparent-wind displacement. Finally, gravity contributes to the displacement in both directions depending on the position along the figure of eight. Table 3 specifies in which direction the tether-kite line is displaced due to gravity for the first five reference instances.
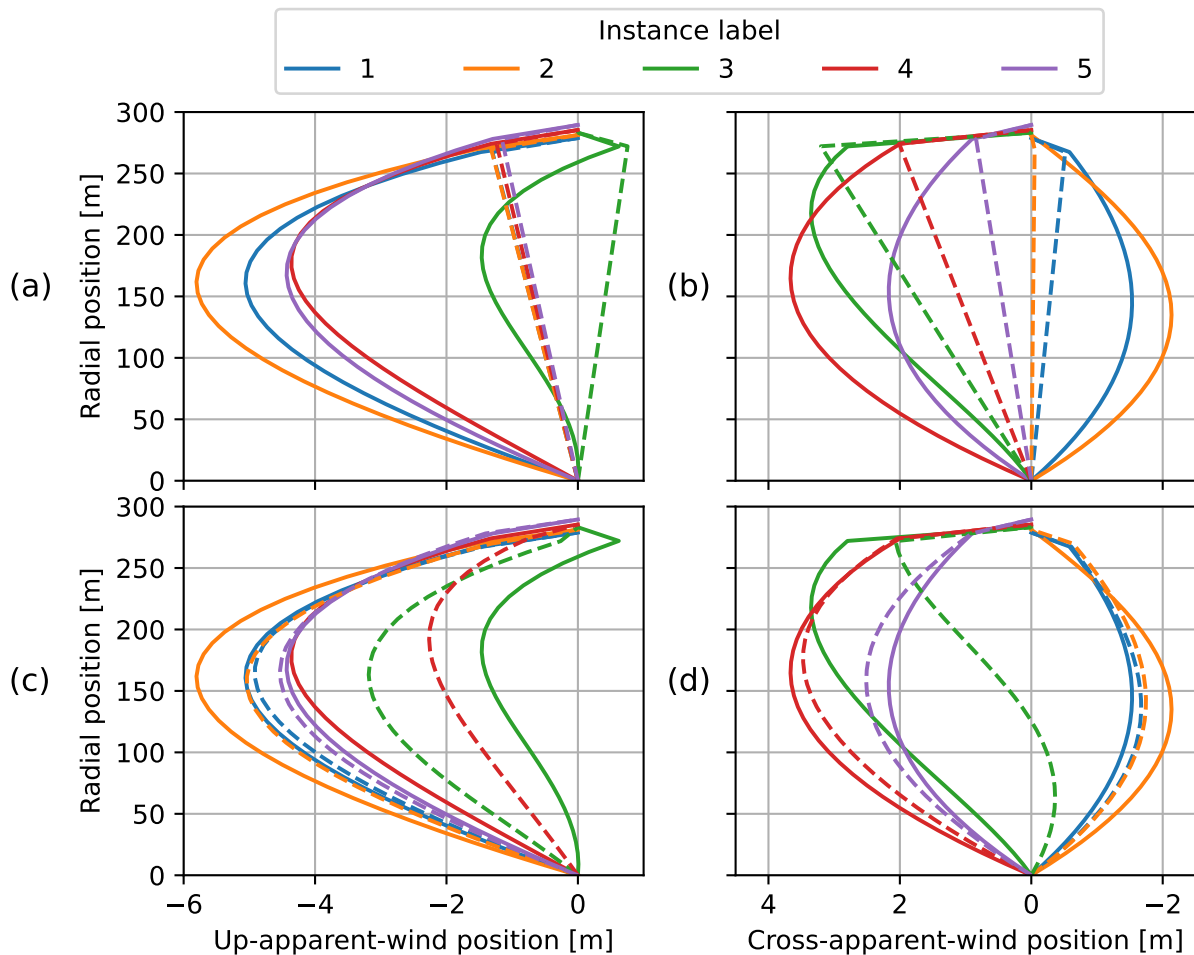
Figure 9. Tether-kite lines with cross-axial displacement expressed with respect to the apparent wind velocity (see Figure 4). Steady-rotation states with 30 tether elements (solid lines in **a**, **b**, **c**, and **d**), with a single tether element (dashed lines in **a** and **b**), and the dynamic solution with 30 tether elements (dashed lines in **c** and **d**) for the first five reference instances. Note that the x- and y-axes have different scales and that the x-axes are flipped in the second column.

The discontinuities in the tether-kite lines at the KCU indicate that it has a substantial effect on the attitude of the kite
265 element. These discontinuities are caused by the high mass and drag that are allocated to the KCU point relative to those lumped to the tether points.

Table 3. Rating the contribution of gravity on the cross-axial displacement of the tether-kite line, ranging from very negative to very positive contributions (−− to ++) in the specified directions with minor contributions left blank.

Instance label	1	2	3	4	5
Up-apparent-wind	-	-	++		-
Cross-apparent-wind	-	-		++	+
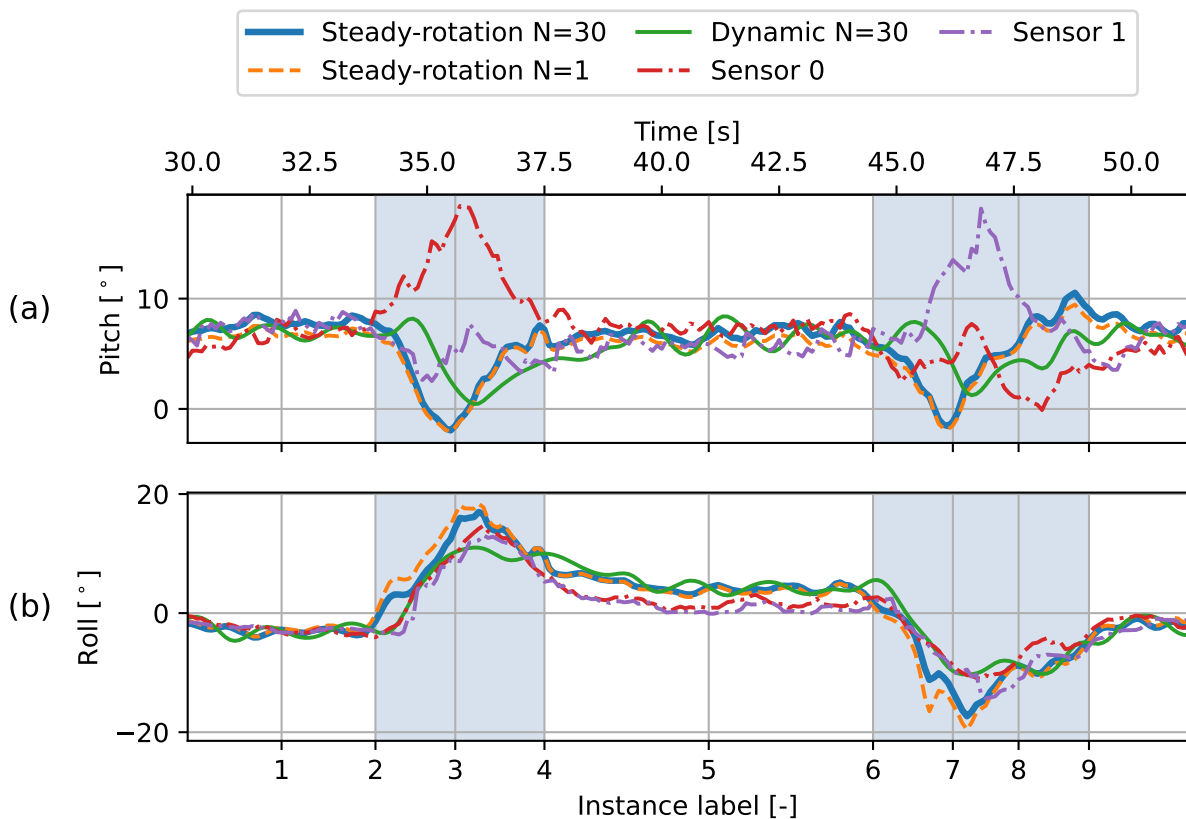
Figure 10. The pitch and roll of the kite element (with respect to the tangential plane) along the figure of eight resulting from the steady-rotation-state and dynamic analyses, together with the kite pitch and roll inferred from the wing attitude measured with the two sensors. The shaded intervals indicate the turns.

To illustrate the imposed kite attitude more clearly, it is quantified using the pitch and roll of the kite element with respect to the tangential plane. The exact definitions are given in Appendix B. Figure 10a shows that the pitch is roughly constant during the straight flight path sections and drops below zero during the turns (blue line). The negative pitch is confirmed by the tether-kite line plot of the 3rd instance in Figure 9a, where the upper kite element is tilted backwards. Note that this depiction

changes when plotting the tether-kite line with respect to, e.g., the vertical instead of the apparent wind velocity. The KCU is actually positioned higher than the wing and can be considered to be pulled along by the wing.

Figure 10b shows a distinct pattern for the roll of the kite along the figure of eight (blue line). The roll is slightly negative, roughly constant at the first straight section flying to the right, whereas it is slightly positive at the subsequent straight section

275 flying to the left. In between, during the right turn, the roll peaks in the middle of the turn at 36.2 s. The left turn shows an opposite pattern. Note that the model does not account for transient effects, which are expected to be substantial during the turns.

The rolling motion of the kite during the turns can be predominantly attributed to the resistance to turn, or inertia, of the KCU. The inertia of the tether has a much smaller effect on the roll. This stresses the need for including a separate point mass

280 for the KCU when assessing the kite attitude.

The analysis is repeated using a single tether element. Figure 9a and b show the resulting tether-kite lines with the dashed lines. As expected, this minimal model is not able to give a good estimation of the maximum displacements. Nevertheless, the resulting kite elements align well with the results of the model with 30 tether elements. Figure 10 confirms this alignment as both the pitch and roll are similar for the two discretisations.

285 ## 4.2 Cross-check with dynamic results

The dynamic simulation requires the wing acceleration prescribing the flight path and tether reel-out acceleration as input. The flight trajectory is reconstructed as described in Appendix A to ensure that these inputs are consistent with the studied figure-of-eight manoeuvre. The reconstruction yields a slightly adapted tether reel-out speed with respect to the measured speed and imposes a constant tether slack in the simulation. The tether slack is set by the choice for the initial tether length of

290 the simulation. A tether slack of 0.3 m is chosen based on the tether lengths resulting from the steady-rotation-state analysis.

Figure 11 shows the tether force evolution that results from the dynamic simulation. The measured force shows distinct peaks during the turns, whereas the simulated force shows a more gradual increase. Otherwise, the measured and simulated forces agree well. The force is very sensitive to the choice of the tether slack. The agreement with measurements confirms that the choice for the constant tether slack is reasonable.

295 The resulting tether-kite lines are plotted in Figure 9c and d. Most shapes of the reference instances show a reasonable agreement with the steady-rotation-state results. An apparent outlier is the 3rd reference instance, which occurs at the outside of the turn. This discrepancy can also be observed in Figure 10a, in which the pitch resulting from the dynamic simulation closely follows the steady-rotation-state model results, except for the middle of the turn. Note that the dynamic model does not include any damping, which could explain the fluctuations in the calculated pitch and roll angles.

300 In principle, the dynamic model should be more suitable than the steady-rotation-state analysis to evaluate the flight behaviour during turns as it concerns a highly dynamic manoeuvre with transient effects on the tether-kite line. These transient effects are likely to explain why in Figure 9d the lower end of the tether of the 3rd reference instance still has a negative cross-apparent-wind displacement like its predecessor, while the corresponding steady-rotation-state result is positive over the
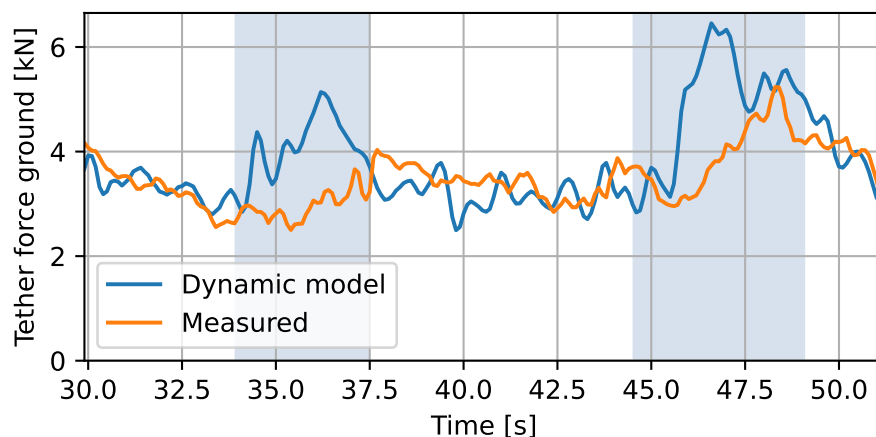
Figure 11. Tether force evolution along the figure of eight resulting from the dynamic simulation and from the flight data. The shaded intervals indicate the turns.

full length. Note that the dynamic model does not necessarily enhance accuracy by considering transient effects as it requires
305 different assumptions, e.g. on the tether reel-out acceleration, with associated uncertainties.

4.3 Kite attitude validation

The available measurements useful for validating the motion of the tether-kite line are the wing attitude measurements. These allow for estimating the actual pitching and rolling motion of the kite and, thereby, can help with validating the models. Validating the rotational motion of the kite is particularly important for performance model development, as accurate descriptions
310 of this motion are essential for incorporating the aerodynamics and the turning mechanism. The tether motion cannot be validated as no measurements are taken directly from the tether. Validating the tether motion is considered less important for performance model development.

The modelled pitch and roll angles of the kite element are compared with measurements from two different sensors mounted to the wing. The same pitch and roll definitions are used to express the wing attitude measurements, provided in Appendix B.
315 The kite attitude is inferred from these measurements by assuming that the kite is fully rigid and that the orientation of the wing relative to the bridle is defined by the depower angle α_d shown in Figure 3. Moreover, the measurements are corrected for misalignments with the wing reference frame. 7° is added to the measured pitch of both sensors to correct for the sensor misalignment. Similarly, 8.5° is subtracted from the roll of both sensors to correct for sensor misalignment.

Both sensors measure a similar roll along the whole figure of eight, as can be seen in Figure 10. However, the pitch measured
320 with the two sensors differs substantially during the turns. Investigating the root cause revealed a strong relationship between the difference in pitch and the steering input. Figure 12c illustrates their relation within the 65th pumping cycle that has a Pearson correlation coefficient of -0.96. A steering input causes the steering tape to pull in on one side and give slack on the other. As a result, the wing twists around the leading edge with zero twist at the centre. The high correlation found suggests

that the twist between the struts on which the sensors are mounted is measured with high precision. The pitch at the centre of
325 the wing is assumed to be the average of the two measurements.
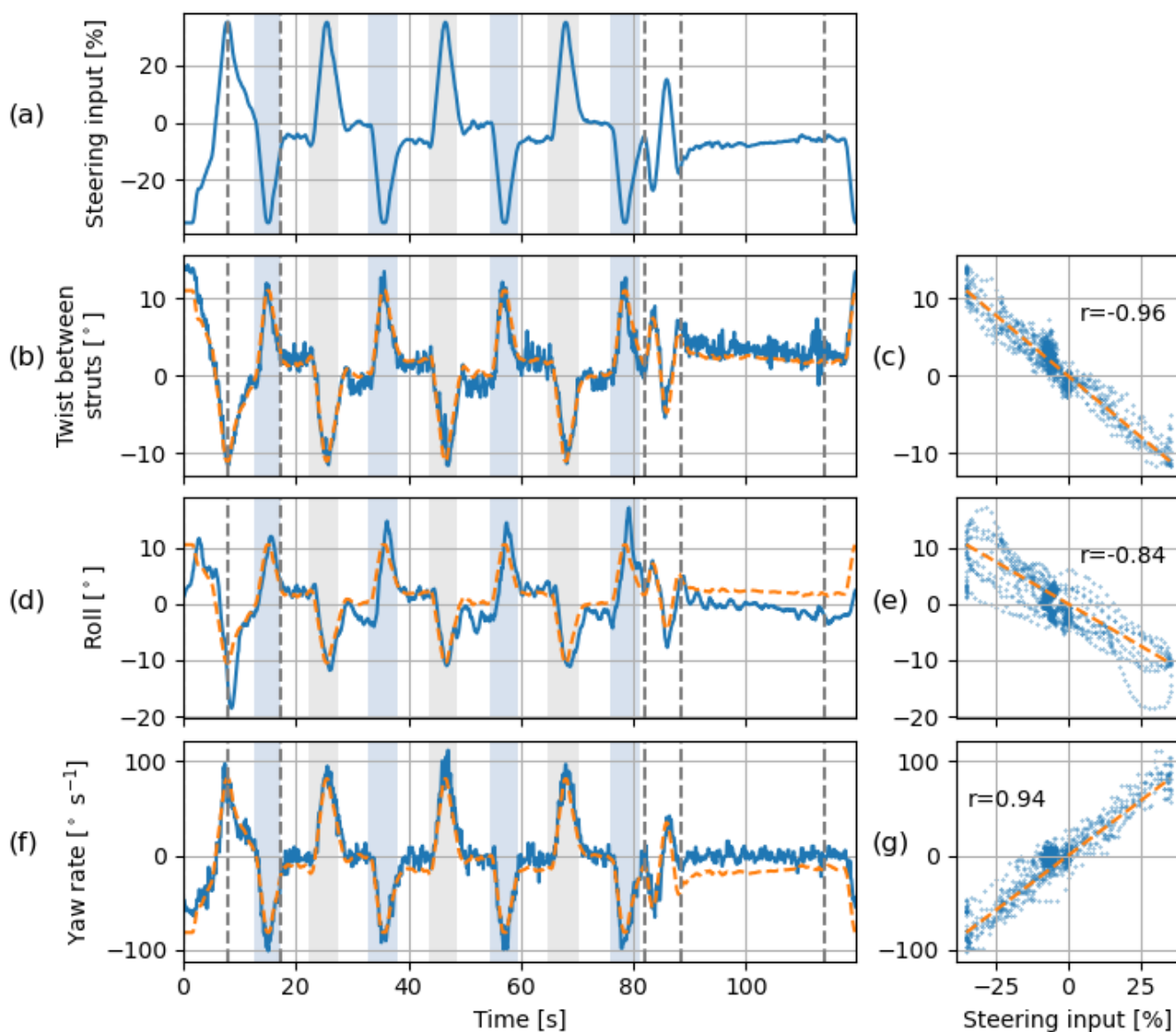
Figure 12. Relations between (**a**) the steering input and (**b, c**) the difference in pitch of the two sensors, (**d, e**) roll of the kite, and (**f, g**) yaw rate of the kite in the 65th pumping cycle. The orange dashed lines in the left column depict the steering input scaled with the slope found in the linear fit shown with the orange dashed lines in the right column.

Figure 10 shows that the differences in pitch and roll resulting from the models and the measurements are small during the straight sections. The computed pitch and roll angles match the measurements within three degrees. Contrastingly, the two models exhibit systematic differences during the turns. In particular, the pitch exhibits larger differences during the turns. Although the dynamic result lies closer to the average measured pitch during the turns, it does not exhibit a similar peak. This discrepancy could be attributed to the high uncertainty of the position measurement during the turns resulting in large modifications to the flight trajectory by the reconstruction. Thereby, the actual wing motion that is causing the peak in pitch might got lost in the reconstruction or was not properly measured. Moreover, the steady-rotation states might not accurately capture the kite attitude during turns because they do not consider transient effects.

In general, the steady-rotation states perform reasonably well in estimating the kite attitude, both with a single and 30 tether elements. This suggests that both discretisations can capture the inertial effect of the KCU during turns. The dynamic model does not necessarily produce more accurate results than the steady-rotation-state model. This can be explained by inaccuracies in the input causing errors, e.g., due to imperfections of the flight trajectory reconstruction.

4.4 Pitching Motion Along a Full Pumping Cycle

To study the pitching motion of the kite outside the reel-out phase, we zoom out and evaluate multiple pumping cycles, including the 65th cycle, which contains the previously investigated figure-of-eight manoeuvre. During the reel-in phase, the kite turns less, and the associated rolling motion is small. Contrastingly, the pitching of the kite induced by tether sag is more pronounced as the tether tension reduces and the weight and drag of the tether are relatively large. Both the weight and drag of the tether result in the tether sagging downwards.

Figure 13 shows the kite pitch inferred from the wing measurements and the kite pitch resulting from the steady-rotation-state analysis with 30 tether elements. The results of ten consecutive pumping cycles are depicted, starting with the 65th pumping cycle. Each cycle starts with the transition into the reel-out phase, followed by approximately four figures of eight. Subsequently, the kite is pointed towards the zenith, depowered, and reeled back in (after the last shaded interval). The cycle ends after powering up again in preparation for a new cycle.

Each cycle shows an increase in pitch after the last turn in the reel-out phase as the kite transitions into the reel-in phase. The model overestimates the pitch at the start of the reel-in and underestimates it towards the end but gives a good overall agreement. There are many factors that may cause this discrepancy. One plausible explanation is that the reduced load during the reel-in phase causes the kite to deform. The deformation is measured but not accounted for in the model and, thus, not incorporated in the computed results. Note that during the reel-in, the steering input is non-zero, as shown in Figure 12a. This causes a pitch offset between the two sensors.

5 Discussion

In this section, we discuss the implications of the observed swinging motion for the performance modelling of a kite system. Different mechanisms initiate and drive a turn of a flexible kite system with a suspended control unit. A steering input causes
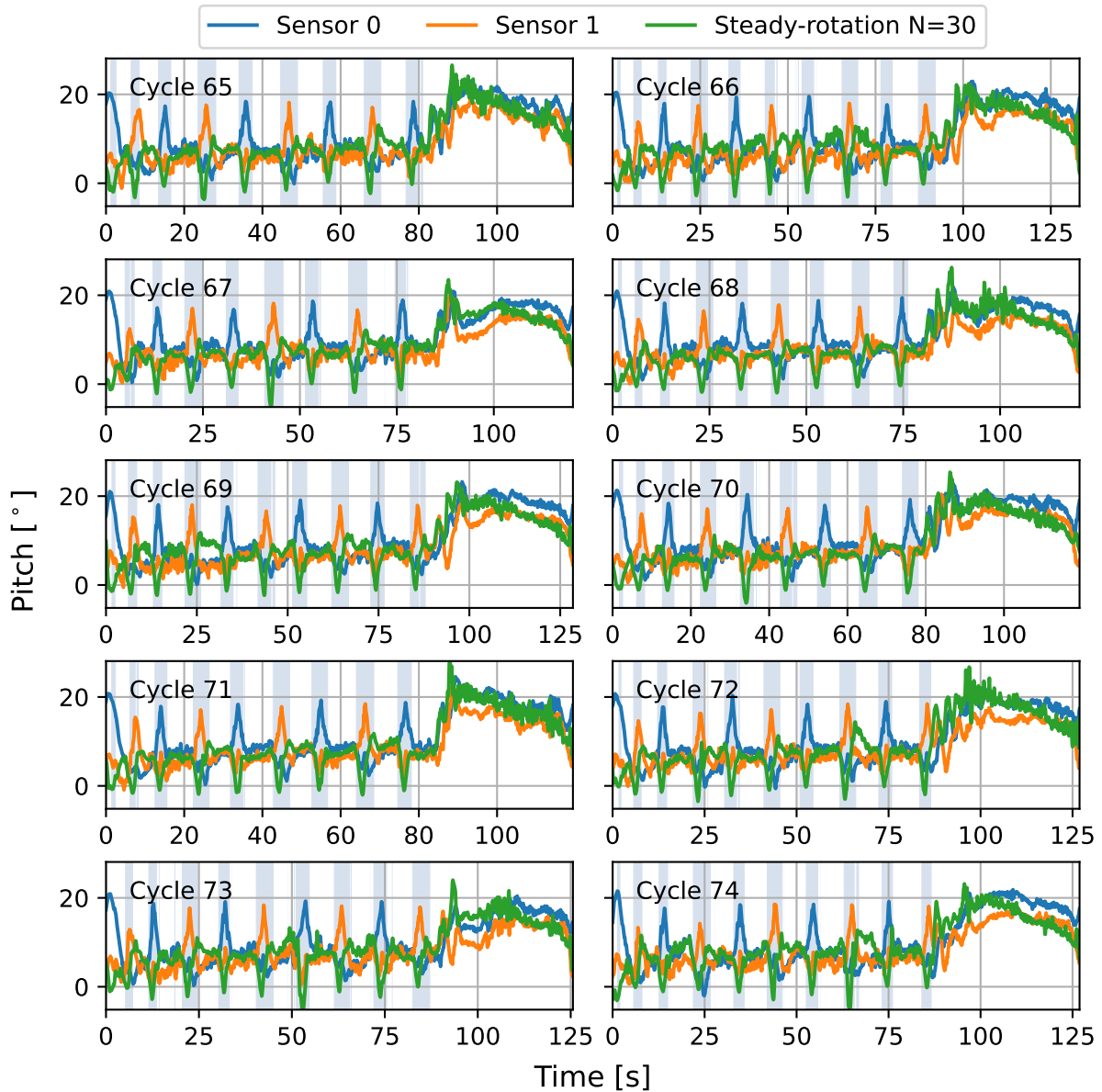
Figure 13. The pitch of the kite element with respect to the tangential plane along ten pumping cycles resulting from the steady-rotation-state analysis using 30 tether elements (T-I N=30), together with the kite pitch inferred from the wing attitude measured with two sensors. The shaded intervals indicate the turns during the reel-out phase. After the turns, the system transitions into the reel-in phase.

the wing to twist, which increases the angle of attack at one tip and decreases it at the other. This creates an aerodynamic side force component perpendicular to the kite symmetry plane and pointing towards the turn centre. This side force component

360   rolls the resultant aerodynamic force acting on the whole kite without rolling the kite itself. Whereas flexible kites with a

suspended control unit rely on this mechanism to initiate the turn, multi-line flexible kites that are actuated from the ground employ it throughout the whole turn. Solely the side force is providing the centripetal force.

As soon as the turn of a flexible kite with a suspended control unit is initiated, the kite starts to roll as it needs to pull the relatively heavy KCU into the turn. The roll of the kite needs to be larger than that of the upper tether end to exert a centripetal

365 force on the KCU. The higher the mass of the KCU, the more roll is required to make it turn. Per definition, the lift force generated by the kite rolls together with the kite and, when rolled, contributes to the centripetal force acting on the KCU. Additionally, the aerodynamic side force is still needed to maintain the turn. However, the rolled lift force is providing the largest contribution to the centripetal force and, thus, is said to drive the turn.

To account for this turning mechanism, a single-point kite model would require substantial simplifications to incorporate the

370 roll of the kite. One option would be to employ an empirical relationship with the steering input shown in Figure 12e. However, with little extra computational cost, the roll can be resolved by modelling the kite with at least two point masses: one for the wing and one for the KCU. Thereby, it no longer needs to rely on system-specific empirical relationships for including the steering mechanism. Instead, the aerodynamic side force needed to initiate and maintain the turn can be calculated based on the deformation of the kite tips and associated aerodynamics.

375 Although the kite pitch does not change substantially during the reel-out phase, the tether-kite motion causes it to change substantially outside this phase. The sag-induced pitch concerns performance modelling as it affects the angle of attack experienced by the wing, which in turn affects the generated aerodynamic forces. Resolving the pitch also requires modelling the kite with at least two point masses and enables incorporating an aerodynamic model for the wing with a dependency on the angle of attack. Complemented with an aerodynamic model of the kite, the dynamic model no longer relies on prescribing the

380 wing acceleration. In contrast to the simulations conducted in the current analysis, simulations that solve the wing motion will be very sensitive to the wind input, which poses a large challenge to the validation of the model.

6 Conclusions

The inertia of the suspended control unit has a large effect on the roll of a flexible kite during turns in the reel-out phase. During the reel-in phase, the pitch of the kite changes due to the weight and drag of the control unit and increased tether sag.

385 These effects are not resolved when the kite is modelled with a single point mass. With two point masses, one at the wing and one at the control unit, the steady-rotation-state model performs reasonably well in capturing the pitch and roll with little extra computational effort. Two-point models can thus be a powerful tool for the performance modelling of flexible kite systems.

The swinging motion of a kite with a suspended control unit is assessed with two approaches: approximated as a transition through steady-rotation states and solved dynamically. The steady-rotation-state model neglects transient effects, whereas the

390 dynamic model solves the actual motion. Both approaches employ a two-point kite model that extends a discretised tether model using an additional rigid element for the kite. By prescribing the cross-wind flight path of the wing, no aerodynamic model of the kite is required.

An alternative expression for the angular velocity underlying the steady-rotation-state approximation is derived that accounts for the turning of the kite. This expression accommodates lateral accelerations on the point masses and, thereby, allows studying

395   the lateral swinging motion of the kite. The expression yields a substantially better approximation of the measured velocity and centripetal acceleration of the wing than the angular velocity of the original model.

The tether-kite lines resulting from the steady-rotation states show discontinuities at the junction between the tether and kite. These indicate that the control unit has a substantial effect on the attitude of the kite and stress the need for including a separate point mass for the control unit in performance models for flexible kite systems. The steady-rotation states perform

400   reasonably well in estimating the roll of the kite, both with a single and 30 tether elements. The computed pitch and roll angles match the measured angles within three degrees during the straight sections of the figure-of-eight manoeuvre. During the turns, the differences in roll may exceed five degrees, whereas the pitch exhibits more systematic differences. These systematic differences could partially be explained by the fact that the model did not account for transient effects. However, a definite conclusion cannot be drawn as the measurements include steering-induced pitch, which impedes a fair comparison.

405   Although the dynamic model considers transient effects, it does not yield more accurate results than the steady-rotation states. This can be explained by inaccuracies in the input causing errors. The dynamic model requires the wing acceleration prescribing the flight path and tether reel-out acceleration as input and is highly sensitive to this input. As the recorded flight trajectory contains anomalies, a reconstruction was needed to produce consistent input. This reconstruction introduces the additional assumption that the tether slack length remains constant.

410   Two separate mechanisms have been identified that initiate and drive a turn of a flexible kite system with a suspended control unit. A steering input causes an aerodynamic side force that initiates the turn. As soon as the turn is initiated, the kite starts to roll as it needs to pull the relatively heavy control unit into the turn. The rolled lift force lying in the symmetry plane of the kite is providing the largest contribution to the centripetal force and is said to drive the turn. Since a two-point kite model resolves the roll, the lift force may tilt along with the kite to drive turns. Hence, it avoids intricate centripetal force modelling, as seen in

415   a single-point kite model. Furthermore, by resolving the pitch, it allows computing the angle of attack of the wing. The angle of attack is important input to the aerodynamic model required when solving the wing motion instead of prescribing a flight path as done in the current study.

Data availability. The complete test flight data including 87 pumping cycles spanning a total flight time of 265 minutes is available in open access from Schelbergen et al. (2023). The specific pumping cycle underlying this study and the Python code for the data analysis is available

420   in open source from Schelbergen.

Appendix A: Flight Trajectory Reconstruction

The kinematics of the wing recorded in the flight data shows inconsistencies in the measured tether reel-out speed and is reconstructed in a preprocessing step to remove anomalies. The dynamic simulation relies on the recorded wing kinematics

and tether reel-out speed for its input. Directly inferring the input from these recorded quantities leads to faulty simulations
425 and a workaround is needed to obtain coherent input. The reconstruction is carried out for the full 65th pumping cycle.

A preliminary evaluation of the wing kinematics in the flight data shows that the vertical speed does not fully agree with
the derivative of the vertical position of the wing, even though it does for the horizontal components. The largest mismatch
occurs during the turns, where the recorded vertical speed is more negative than the derivative of the vertical position. The
recorded vertical position is GPS data enhanced with barometer measurements. However, we expect that the vertical speed is
430 not updated accordingly.

The inconsistent vertical speed leads to a discrepancy between the radial component of the wing velocity and the derivative
of the radial position, while in theory, they should be the same. Both are shown in Figure A1c. The radial component of the
wing velocity is calculated with:

$$v_{s,r} = \frac{\mathbf{r}_s^T \mathbf{v}_s}{\|\mathbf{r}_s\|}, \tag{A1}$$

435 in which $\mathbf{r}_s$ and $\mathbf{v}_s$ are the position and velocity of the wing, respectively. The flight trajectory reconstruction needs to as-
sure consistency between the kinematic properties such that also the updated radial component of the wing velocity and the
derivative of the radial position will agree.

As an additional check, the derivative of the radial position of the wing is compared to the reel-out speed. The derivative
of the radial position shows large fluctuations around the tether reel-out speed in the reel-out phase. The magnitude of the
440 fluctuations conflicts with our expectation that the changes in tether slack and stretch are small in this phase. Towards the end
of the turns, the derivative of the radial position even tends to become shortly negative, which coincides with the subtle local
maxima found at the end of the blue intervals in the recorded radial position in Figure A1a.

Figure A1a shows how the integrated measured reel-out speed (dotted black line) evolves with respect to the recorded radial
position of the wing (blue line). During the right turns, the inferred tether length stays increasing roughly linearly, while the
445 radial position shows local maxima. Note that the lines need to be shifted up with their initial values to obtain their respective
absolute values. Unfortunately, we do not know the absolute tether length as it is not measured directly.

The residual between the inferred tether length and recorded radial position is shown in Figure A1b. During the right turns,
the residual changes roughly 2 m (depth of the valley) within a couple of seconds. The corresponding relatively large increase
in radial position can partly be attributed to a decrease in tether slack and an increase in tether stretch. However, the magnitude
450 of the change is deemed to be too large to be attributed only to tether dynamics. Note that also here, the line may shift vertically
depending on the initial values. As such, we can not draw conclusions based on the magnitude of the residual but merely on
how it changes with time. The sum of the residual length and an unknown offset gives an approximation of the tether slack.
The true tether slack also accounts for tether stretch, which is not accounted for in calculating the residual length. Note that the
tether slack can not be negative.

455 The maxima in the recorded radial position do not need to be purely physical. Another possible cause is GPS inaccuracy
during manoeuvres, which has previously been reported in the literature. Borobia et al. (2018) reported measured radial position
exceeding varying more than 3 m while none was expected. Considering the imprecision of the recorded position, we opt for
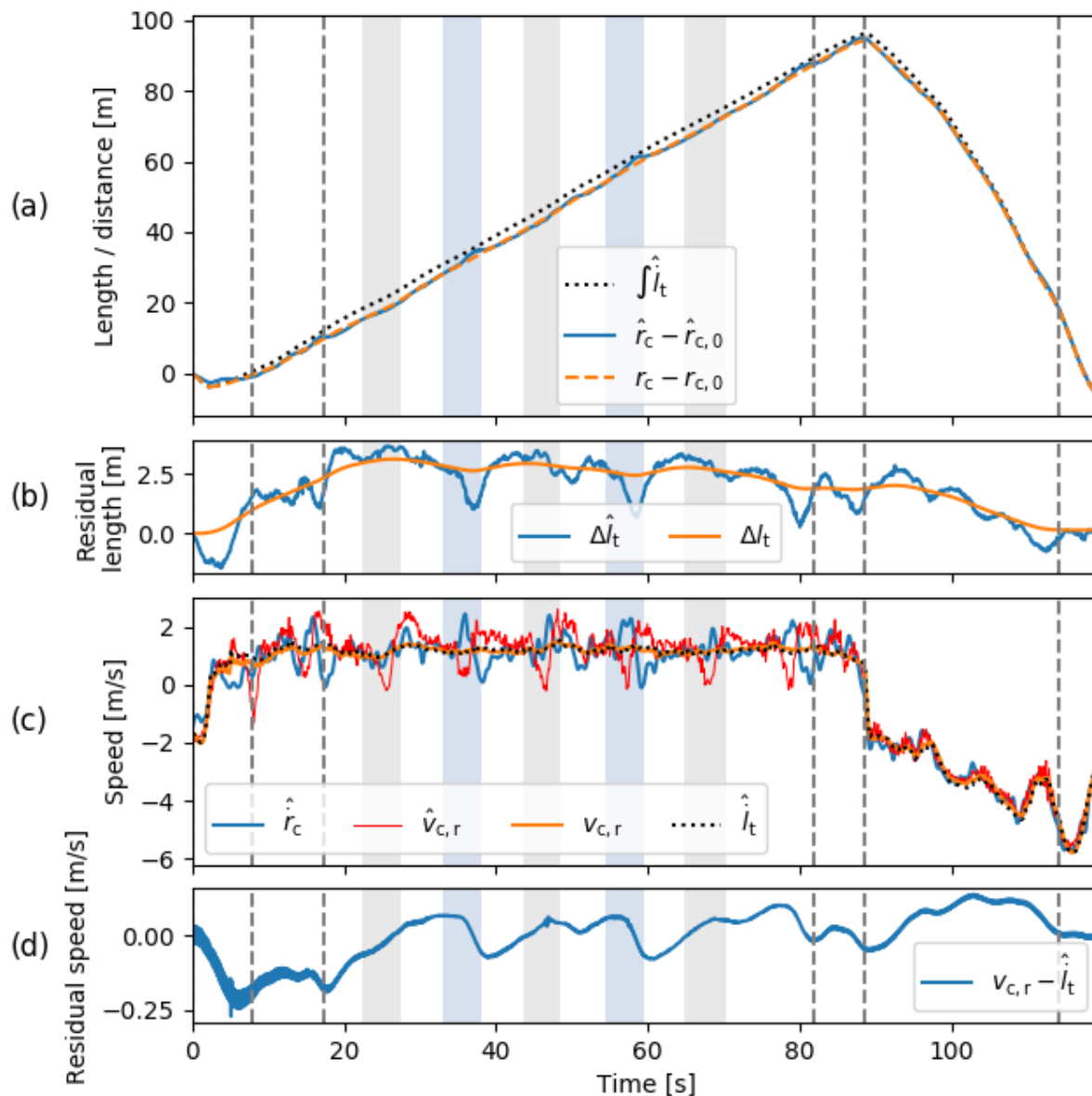
Figure A1. (**a**) Evolution of unstrained tether length and the recorded and reconstructed radial distances of the wing, all with their initial values subtracted. (**b**) Difference between the tether length and radial distance. (**c**) Measured tether reel-out speed and recorded and reconstructed radial speeds of the wing. (**d**) Residual between the reel-out speed and reconstructed radial speed. The intervals shaded grey and blue indicate left and right turns, respectively, from a downwind perspective.

adapting the wing kinematics and letting the tether reel-out acceleration input follow the measured reel-out speed as closely as possible.

460   The flight trajectory reconstruction is obtained using an optimal control problem that minimises the error between the modelled radial wing speed and recorded tether reel-out speed while limiting the bias between the modelled and recorded wing position

$$
\min_{\mathbf{r}_s, \mathbf{v}_s, \mathbf{a}_s, r_{s,r}, v_{s,r}, a_{s,r}} \sum_{i=0}^{N} \left[w \left(v_{s,r} - \hat{\dot{l}}_t \right)^2 + \left(\mathbf{r}_s - \hat{\mathbf{r}}_s \right)^T \left(\mathbf{r}_s - \hat{\mathbf{r}}_s \right) \right]_{t=\frac{i}{10}}
$$
$$
\text{s.t.} \quad \mathbf{a}_s = \dot{\mathbf{v}}_s = \ddot{\mathbf{r}}_s \qquad\qquad ; \tag{A2}
$$
$$
a_{s,r} = \dot{v}_{s,r} = \ddot{r}_{s,r}
$$
$$
r_{s,r} = \|\mathbf{r}_s\|
$$

in which the hat denotes a measured quantity; the discrete control input trajectories $\mathbf{a}_s$ and a_r are the wing acceleration and
465 its radial component; $\mathbf{v}_s$, v_r, $\mathbf{r}_s$, and r_r describe the corresponding trajectories of the velocity and position; $\hat{\dot{l}}_t$ is the measured tether reel-out speed; N is the number of time steps; and the weighing factor w = 25 is chosen as it leads to a good balance between the two objectives. Note that having matching reel-out and radial wing speeds does not necessarily mean that also the tether length is the same as the radial position. However, it does mean that the tether slack stays constant.

    In line with the dynamic simulation, the fitting problem uses discrete control input trajectories. It assumes a constant ac-
470 celeration within each simulation time step of 0.1 s. Between the corresponding control intervals, the values may vary. Due to the step function form of the acceleration, the velocity and position are linear and quadratic functions, respectively, within the control intervals. These low-order forms allow for sufficient detail due to the small time step, provided that integration drift along the trajectory is prevented by the fitting, i.e., the fitting prevents an accumulating error with time. The problem is solved in CasADi using a multiple-shooting approach.

475   The flight trajectory reconstruction results are shown with the orange lines in Figure A1. The reconstruction shaves off the local maxima in the recorded radial position as can be observed in Figure A1a. Figure A1c shows that the reconstructed radial wing speed follows the measured reel-out speed more closely. The residual speed, which is penalised by the first term of the objective function, is illustrated in Figure A1d. The optimiser reduces the position bias, which is penalised by the second term of the objective function, by allowing small changes to the radial wing speed with respect to the measured reel-out speed. As
480 a consequence, the reconstruction does not lower the residual length substantially but keeps it close to the original residual length, as can be seen in Figure A1b.

    We use $a_{s,r}$ as tether reel-out acceleration input for the simulation. Effectively we thus do not only reconstruct the flight trajectory but also modify the tether reel-out speed with respect to the measurements. As a result, the tether slack remains constant in the simulation and is set by the choice for the initial tether length. In reality, changes in slack length will occur,
485 especially during the transition phases. Therefore, this approach might be sub-optimal for simulating the entire pumping cycle. Nonetheless, it is suitable for simulating intervals where only small tether slack and stretch changes are expected, such as the reel-out phase.

We acknowledge that the flight trajectory reconstruction might not be strictly valid. Nevertheless, it serves the higher aim of this study and allows simulating a short interval which encompasses a figure of eight during reel-out. A more educated recon-
490 struction would require a lot more resources and probably more testing and is recommended as a possible future improvement.

Appendix B: Pitch and Roll Angle Definitions

Expressing the attitude of the kite using pitch and roll angles with respect to the wind reference frame gives large variations of these angles along the flight trajectory. Consequently, the kite attitude is difficult to interpret from these angles. Variations are smaller when the pitch and roll angles are expressed with respect to the tangential plane, which is perpendicular to the position
495 vector of the kite and shown with the black rectangle in Figure B1. The variations are smaller since the up-direction (positive z-axis) of the kite and the direction of the position vector in the wind reference frame are not far apart, especially during the reel-out phase, where the tether is relatively straight due to the high pulling force of the kite.

B1 Measured attitude of the kite

The rotation matrix for the transformation from the wind to the tangential reference frame is calculated by:

500 $$\mathbb{T}_{\tau e} = \begin{bmatrix} \sin\hat{\beta} & 0 & -\cos\hat{\beta} \\ 0 & 1 & 0 \\ \cos\hat{\beta} & 0 & \sin\hat{\beta} \end{bmatrix} \begin{bmatrix} \cos(\hat{\varphi}+\hat{\varphi}_{\mathrm{we}}) & \sin(\hat{\varphi}+\hat{\varphi}_{\mathrm{we}}) & 0 \\ -\sin(\hat{\varphi}+\hat{\varphi}_{\mathrm{we}}) & \cos(\hat{\varphi}+\hat{\varphi}_{\mathrm{we}}) & 0 \\ 0 & 0 & 1 \end{bmatrix},$$ (B1)

in which subscripts τ, w, and e refer to the tangential, wind, and earth reference frames, respectively, the hat denotes a measured quantity, β is the elevation angle, and φ is the azimuth angle.

The measured pitch, roll, and yaw of the wing of the kite are expressed using 3-2-1 Euler angles. The corresponding rotation matrix for the transformation from the earth to the wing reference frame is calculated by:

505 $$\mathbb{T}_{se} = \begin{bmatrix} 1 & 0 & 0 \\ 0 & \cos\hat{\phi} & \sin\hat{\phi} \\ 0 & -\sin\hat{\phi} & \cos\hat{\phi} \end{bmatrix} \begin{bmatrix} \cos\hat{\theta} & 0 & -\sin\hat{\theta} \\ 0 & 1 & 0 \\ \sin\hat{\theta} & 0 & \cos\hat{\theta} \end{bmatrix} \begin{bmatrix} \cos\hat{\psi} & \sin\hat{\psi} & 0 \\ -\sin\hat{\psi} & \cos\hat{\psi} & 0 \\ 0 & 0 & 1 \end{bmatrix},$$ (B2)

in which subscripts c and e refer to the wing and earth reference frames, respectively, ϕ is the roll angle, θ is the pitch angle, and ψ is the yaw angle.

The attitude of the kite is not affected by the depower signal and can be approximated by pitching the wing reference frame with the negative of the depower angle α_{d} depicted in Figure 3

510 $$\mathbb{T}_{bs} = \begin{bmatrix} \cos\alpha_{\mathrm{d}} & 0 & \sin\alpha_{\mathrm{d}} \\ 0 & 1 & 0 \\ -\sin\alpha_{\mathrm{d}} & 0 & \cos\alpha_{\mathrm{d}} \end{bmatrix},$$ (B3)

in which subscript b denotes the bridle reference frame. The depower angle is calculated using a geometrical model from the power setting (Schelbergen and Schmehl, 2020) and yields a nose down pitch angle of roughly 6.6° during the reel-in phase.
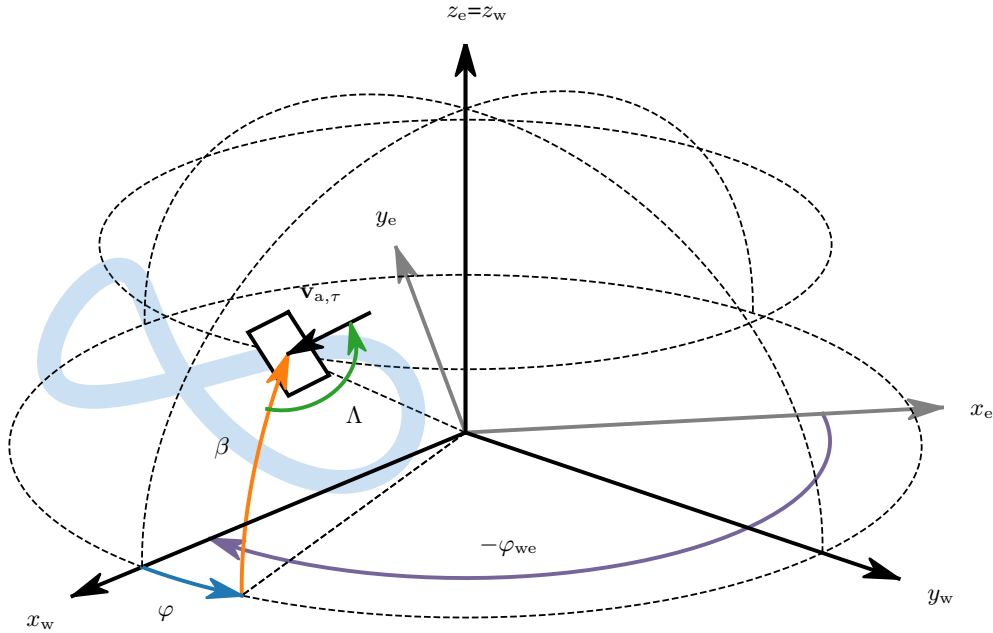
Figure B1. Earth reference frame $x_\mathrm{e}, y_\mathrm{e}, z_\mathrm{e}$ and wind reference frame $x_\mathrm{w}, y_\mathrm{w}, z_\mathrm{w}$ together with the yawed tangential plane lying on the projection of a figure-of-eight flight path. This plane is yawed such that it heads into the apparent wind velocity and serves as a departure point for expressing the kite attitude, illustrated in Figure B2. The corresponding yaw angle Λ is equal to the kite heading in case of zero side slip.

The rotation matrix for the transformation from the tangential to the bridle reference frame is derived from the previously presented matrices:

$$\mathbb{T}_\mathrm{bs}\,\mathbb{T}_\mathrm{se}\,\mathbb{T}_{\tau\mathrm{e}}^T = \mathbb{T}_\mathrm{bs}\,\mathbb{T}_\mathrm{se}\,\mathbb{T}_{\mathrm{e}\tau} = \mathbb{T}_{\mathrm{b}\tau}\,. \tag{B4}$$

Only a single set of 3-2-1 Euler angles exists that produces a rotation matrix. The corresponding yaw, pitch, and roll can be calculated using the lower expressions:

$$\psi = \arctan2\left(\mathbb{T}_{12}, \mathbb{T}_{11}\right), \tag{B5}$$

$$\theta = -\arctan2\left(\mathbb{T}_{13}, \sqrt{\mathbb{T}_{23}^2 + \mathbb{T}_{33}^2}\right), \tag{B6}$$

$$\phi = \arctan2\left(\mathbb{T}_{23}, \mathbb{T}_{33}\right), \tag{B7}$$

in which $\mathbb{T}_{ij}$ denotes the transformation matrix element at the ith row and j^th column. The Euler angles corresponding to $\mathbb{T}_{\mathrm{b}\tau}$ are denoted without a subscript. The definitions of the pitch and roll angles are illustrated in Figure B2, taking the yawed tangential plane as the point of departure.

Λ in Figure B1 describes the orientation of the tangential projection of the modelled apparent wind velocity, also shown in Figure 4. In case of no side slip, Λ is equal to the heading angle. The heading angle inferred from measurements and Λ
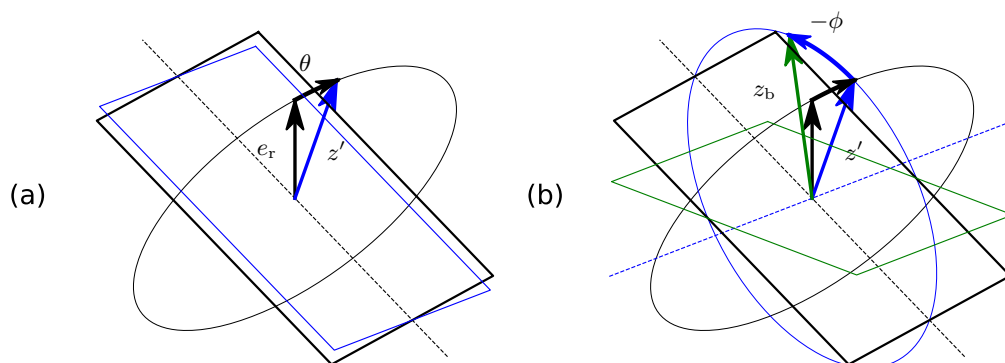
Figure B2. Last two rotations in the 3-2-1 sequence (Euler angles) to get from the tangential to the bridle reference frame: (**a**) a positive pitch rotation and (**b**) a negative roll rotation. The black rectangle illustrates the yawed tangential plane, introduced in Figure B1.

have a small periodic misalignment (not plotted), which may indicate side slip. However, the constant wind assumption and measurement errors introduce too much uncertainty to confirm this. Also, the side slip angle was not measured in the studied test flight and thus can not be validated. Nevertheless, some side slip can be expected as has previously been shown in the experiments by Oehler and Schmehl (2019).

530 **B2 Modelled attitude of the kite**

Expressing the Euler angles of the kite element of the model requires assigning a local reference frame to the element. The model does not specify a full reference frame but only specifies the axial direction of the element. This axial direction is used as the z-axis for the local reference frame. To differentiate between the roll and pitch, also the x-axis and y-axis need to be specified. The x-axis is chosen such that it lies in the plane spanned by the position vector and the vertical direction z_e. The
535 y-axis then follows from the other two axes and is oriented horizontally.

Other than for securing the alignment between the roll and pitch definitions of the measured and modelled kite attitude, the yaw of the tether is not of interest to this study. It does not affect the kite attitude itself and, therefore, the resulting yaw angles are left out of Figure 10. The modelled yaw of the kite is similar to that inferred from the wing attitude measurements and, thereby, facilitates comparing the measured and modelled roll and pitch.

540 *Author contributions.* Conceptualisation, M.S. and R.S.; methodology, M.S.; software, M.S.; investigation, M.S.; writing—original draft preparation, M.S.; writing—review and editing, R.S.; supervision, R.S.; funding acquisition, R.S. All authors have read and agreed to the published version of the manuscript.

Competing interests. Roland Schmehl is a member of the editorial board of Wind Energy Science. He also is a co-founder of and advisor for the start-up company Kitepower B.V., which is commercially developing a 100 kW kite power system and provided their test facilities

545 and staff for performing the in situ measurements described in this article. Both authors were financially supported by the European Union's Horizon 2020 project REACH, which also provided funding for Kitepower B.V.

Acknowledgements. This research was part of the project REACH (H2020-FTIPilot-691173), funded by the European Union's Horizon 2020 research and innovation programme under grant agreement No. 691173, and the project AWESCO (H2020-ITN-642682) funded by the European Union's Horizon 2020 research and innovation programme under the Marie Skłodowska-Curie grant agreement No. 642682.

550 The authors are grateful to Kitepower B.V. for making the flight data available in open access and for sharing expertise about the system, in particular Joep Breuer for asking critical questions. Also, we would like to thank Arthur Roullier on whose MSc thesis this work builds upon and Jochem de Schutter for his tips on implementing the dynamic simulation.

References

Andersson, J. A. E., Gillis, J., Horn, G., Rawlings, J. B., and Diehl, M.: CasADi – A software framework for nonlinear optimization and optimal control, Mathematical Programming Computation, 11, 1–36, https://doi.org/10.1007/s12532-018-0139-4, 2019.

Borobia, R., Sanchez-Arriaga, G., Serino, A., and Schmehl, R.: Flight-Path Reconstruction and Flight Test of Four-Line Power Kites, Journal of Guidance, Control, and Dynamics, 41, 2604–2614, https://doi.org/10.2514/1.G003581, 2018.

Bosch, A., Schmehl, R., Tiso, P., and Rixen, D.: Nonlinear Aeroelasticity, Flight Dynamics and Control of a Flexible Membrane Traction Kite, in: Airborne Wind Energy, edited by Ahrens, U., Diehl, M., and Schmehl, R., Green Energy and Technology, chap. 17, pp. 307–323, Springer, Berlin Heidelberg, https://doi.org/10.1007/978-3-642-39965-7_17, 2013.

Breukels, J., Schmehl, R., and Ockels, W.: Aeroelastic Simulation of Flexible Membrane Wings based on Multibody System Dynamics, in: Airborne Wind Energy, edited by Ahrens, U., Diehl, M., and Schmehl, R., Green Energy and Technology, chap. 16, pp. 287–305, Springer, Berlin Heidelberg, https://doi.org/10.1007/978-3-642-39965-7_16, 2013.

Cayon, O.: Fast aeroelastic model of a leading-edge inflatable kite for the design phase of airborne wind energy systems, Master's thesis, Delft University of Technology, http://resolver.tudelft.nl/uuid:aede2a25-4776-473a-8a75-fb6b17b1a690, 2022.

Duport, C.: Modeling with consideration of the fluid-structure interaction of the behavior under load of a kite for auxiliary traction of ships, Phd thesis, ENSTA Bretagne, https://tel.archives-ouvertes.fr/tel-02383312, 2018.

Fagiano, L., Quack, M., Bauer, F., Carnel, L., and Oland, E.: Autonomous Airborne Wind Energy Systems: Accomplishments and Challenges, Annual Review of Control, Robotics, and Autonomous Systems, 5, https://doi.org/10.1146/annurev-control-042820-124658, 2022.

Fechner, U., van der Vlugt, R., Schreuder, E., and Schmehl, R.: Dynamic Model of a Pumping Kite Power System, Renewable Energy, 83, 705–716, https://doi.org/10.1016/j.renene.2015.04.028, 2015.

Folkersma, M. A. M.: Aeroelasticity of Membrane Kites: Airborne Wind Energy Applications, Ph.D. thesis, Delft University of Technology, Delft, https://doi.org/10.4233/uuid:eae39f5a-49bc-438b-948f-b6ab51208068, 2022.

Geschiere, N.: Dynamic modelling of a flexible kite for power generation, Master's thesis, Delft University of Technology, http://resolver.tudelft.nl/uuid:6478003a-3c77-40ce-862e-24579dcd1eab, 2014.

Gohl, F. and Luchsinger, R. H.: Simulation based wing design for kite power, in: Airborne Wind Energy, edited by Ahrens, U., Diehl, M., and Schmehl, R., Green Energy and Technology, chap. 18, pp. 325–338, Springer, Berlin Heidelberg, https://doi.org/10.1007/978-3-642-39965-7_18, 2013.

Kitepower B.V.: Onshore Containerised AWES-100 Kitepower Falcon, https://thekitepower.com/product/.

Loyd, M. L.: Crosswind kite power, Journal of Energy, 4, 106–111, https://doi.org/10.2514/3.48021, 1980.

Oehler, J. and Schmehl, R.: Aerodynamic characterization of a soft kite by in situ flow measurement, Wind Energ. Sci., 4, 1–21, https://doi.org/10.5194/wes-4-1-2019, 2019.

Oehler, J., van Reijen, M., and Schmehl, R.: Experimental Investigation of Soft Kite Performance During Turning Maneuvers, Journal of Physics: Conference Series, 1037, 052 004, https://doi.org/10.1088/1742-6596/1037/5/052004, 2018.

Peschel, J., Breuer, J., and Schmehl, R.: Kitepower – Commercializing a 100 kW Mobile Wind Energy System, in: Book of Abstracts of the International Airborne Wind Energy Conference (AWEC 2017), edited by Diehl, M., Leuthold, R., and Schmehl, R., pp. 47–51, University of Freiburg | Delft University of Technology, Freiburg, Germany, http://resolver.tudelft.nl/uuid:9e9a6bdb-f5f4-4868-bed6-f25dc5ee42f0, 2017.

Poland, J.: Modelling aeroelastic deformation of soft wing membrane kites, Master's thesis, Delft University of Technology, http://resolver.
    tudelft.nl/uuid:39d67249-53c9-47b4-84c0-ddac948413a5, 2022.

Rapp, S., Schmehl, R., Oland, E., and Haas, T.: Cascaded Pumping Cycle Control for Rigid Wing Airborne Wind Energy Systems, Journal
    of Guidance, Control, and Dynamics, 42, 2456–2473, https://doi.org/10.2514/1.G004246, 2019.

Roullier, A.: Experimental analysis of a kite system's dynamics, Master's thesis, EPFL, https://doi.org/10.5281/zenodo.7752407, 2020.

Salma, V., Friedl, F., and Schmehl, R.: Reliability and Safety of Airborne Wind Energy Systems, Wind Energy, 23, 340–356,
    https://doi.org/10.1002/we.2433, 2019.

Schelbergen, M.: Swinging Motion of a Kite, https://github.com/awegroup/swinging-kite.

Schelbergen, M. and Schmehl, R.: Validation of the quasi-steady performance model for pumping airborne wind energy systems, Journal of
    Physics Conference Series, 1618, 032 003, https://doi.org/10.1088/1742-6596/1618/3/032003, 2020.

Schelbergen, M., Schmehl, R., Buchholz, B., Breuer, J., and Peschel, J.: Kitepower flight data acquired on 8 October 2019, Dataset,
    4TU.Centre for Research Data, https://doi.org/10.4121/19376174, 2023.

Schmehl, R. and Oehler, J.: 25 m^2 LEI V3 tube kite transitioning to traction phase and starting to fly figure eight manoeuvres. Video footage
    of onboard camera, TIB AV Portal, Copernicus Publications, https://doi.org/10.5446/37583, 2018.

Sánchez-Arriaga, G., Pastor-Rodríguez, A., Sanjurjo-Rivo, M., and Schmehl, R.: A lagrangian flight simulator for airborne wind energy
    systems, Applied Mathematical Modelling, 69, 665–684, https://doi.org/10.1016/j.apm.2018.12.016, 2019.

Thedens, P.: An Integrated Aero-Structural Model for Ram-Air Kite Simulations With Application to Airborne Wind Energy, Ph.D. thesis,
    Delft University of Technology, Delft, https://doi.org/10.4233/uuid:16e90401-62fc-4bc3-bf04-7a8c7bb0e2ee, 2022.

Vermillion, C., Cobb, M., Fagiano, L., Leuthold, R., Diehl, M., Smith, R. S., Wood, T. A., Rapp, S., Schmehl, R., Olinger, D., and Demetriou,
    M.: Electricity in the Air: Insights From Two Decades of Advanced Control Research and Experimental Flight Testing of Airborne Wind
    Energy Systems, Annual Reviews in Control, 52, 330–357, https://doi.org/10.1016/j.arcontrol.2021.03.002, 2021.

Williams, P.: Cable Modeling Approximations for Rapid Simulation, Journal of Guidance, Control, and Dynamics, 40, 1779–1788,
    https://doi.org/10.2514/1.G002354, 2017.

Williams, P., Lansdorp, B., and Ockels, W. J.: Modeling and Control of a Kite on a Variable Length Flexible Inelastic Tether, in: Proceedings
    of the AIAA Modeling and Simulation Technologies Conference and Exhibit, Hilton Head, SC, USA, https://doi.org/10.2514/6.2007-
    6705, 2007.

Zanon, M., Gros, S., Andersson, J., and Diehl, M.: Airborne Wind Energy Based on Dual Airfoils, IEEE Transactions on Control Systems
    Technology, 21, 1215–1222, https://doi.org/10.1109/TCST.2013.2257781, 2013.